

DEVELOPMENT AND EXPERIMENTAL ANALYSIS OF A MICRO-FLAME IONIZATION
DETECTOR FOR PORTABLE GAS CHROMATOGRAPHS

BY

JIHYUNG KIM

DISSERTATION

Submitted in partial fulfillment of the requirements
for the degree of Doctor of Philosophy in Mechanical Engineering
in the Graduate College of the
University of Illinois at Urbana-Champaign, 2013

Doctoral Committee:

Professor Dimitrios C. Kyritsis, Chair
Professor Mark A. Shannon, Director of Research
Professor Alexander Scheeline
Professor Placid M. Ferreira
Professor William P. King

Abstract

A portable micro-FID has been developed that utilized a diffusion flame encased in a micro-fabricated SOI structure. The micro-flame was fueled by a portable electrolyzer that provided the hydrogen and oxygen flow rates necessary for the device operation. The micro-FID was able to detect organic analytes with sensitivity that competes with the one of large-scale devices.

A first major accomplishment was the encasement of a stable diffusion flame inside a quartz-silicon-quartz sandwich structure. Several micro-burner configurations were tested by varying the angle between the oxidizer and the hydrogen gas of silicon channels. The final design employed a diffusion flame that was encapsulated inside a 750 μm thick silicon channel. When the streams of oxidizer and hydrogen met at a 150° angle, a single folded flame structure with low flame strain was obtained that minimized analyte loss.

The effect of channel geometry on flame structure was explored using the ANSYS FLUENT computational fluid dynamics (CFD) software package in order to compute the reactive flow in a two-dimensional geometry that simulated the micro-burner channels. Hydroxyl radical (OH) mass fraction distributions were computed as an indicator of the high-temperature zone of the flame. Also, the two-dimensional flow-field was computed in order to determine the strain rate on the non-premixed flamelet, which was used in order to rationalize flame structure. It was determined from the simulation that an angle of convergence between the channels around 150°-160° provided the least analyte loss as well as relatively low strain rates.

In order to verify this experimentally, two different channel configurations, a folded flame channel design (150° angle) and a counter-flow channel design (180° angle) were tested and compared. Methane gas was injected in the hydrogen stream and the resulting ion current was measured. The folded flame channel design produced about 34 times stronger signals compared to the counter-flow channel design. The micro-FID that was based on this configuration had a linear response.

In order to improve signal strength and reduce fuel consumption rate, an oxygen stream was added to the air stream and the overall channel width size was reduced to 50%. Additionally, reducing the dead volume of the injection port and introducing anchor points to the channels improved the overall device performance. These modifications allowed reducing the overall fuel consumption and improved the sensitivity by a factor of about three. In order to increase the sensitivity of the device, not only was the signal strength improved, but also efforts were made to reduce the noise. To this end, channels were fabricated with silicon-on-insulator wafers and the entire micro-FID was tested inside a Faraday cage. These modifications suppressed the noise by a factor of 43 and improved the overall sensitivity and the minimum detection level. Furthermore, it enabled the instrument to detect a mixture of 17 different gas compounds.

The fuel flow rate was varied in order to determine the flow conditions that optimized flame stability and resulted in increased signal-to-noise ratio. Results showed that the highest signal-to-noise ratio was achieved with an air flow of 45 ml/min, a hydrogen flow of 26 ml/min, and an oxygen flow of 13 ml/min. Finally, the saturation voltage of the electrodes was determined in order to avoid unnecessary charge to the battery during operation and it was shown to be very closely equal to 100 V.

Acknowledgements

I would like to thank Prof. Mark A. Shannon for guiding and supporting my research with mentorship and encouragement throughout my studies at University of Illinois at Urbana-Champaign. His passion in research and the love for his students inspired me in many ways. His exceptional insight about physical phenomena always inspired me and motivated my desire to learn.

I am also grateful to Prof. Dimitrios C. Kyritsis for guiding me with the academic and research work. All the opportunities he provided me make my graduate school experience a truly valuable experience. Even during the toughest times he advised me with patience, and generosity. Without his help I would never have been able to come this far.

All the experiments, data plots and results described in Chap. 4 - 7 were performed and obtained using Cbana facilities under Dr. Byunghoon Bae's guidance and support. I deeply appreciate Dr. Taekyu Kang, Dr. Byunghoon Bae, and Dr. Junghoon Yeom for working together. I am also thankful for their endless assistance, suggestion, and support through my research. Thankfully, they have always cared me and spent their time for me to discuss my research and career.

I am lucky and feel grateful to have the opportunity to spend time together with members in Shannon research group. I appreciate Dr. Glennys Mensing for teaching me and working together in the cleanroom. I would like to thank all of my friends and colleagues in Shannon Research Group for valuable discussions and suggestions, to Dr. Bruce Flachsbart, Damena Agonafer, Shama Farabi, Vikhram Vilasur Swaminathan, Yaofeng Chen, Huan Hu, Ahmad Qadi, Ali Ashraf, Cody Jensen, and Andrea Vozar.

Most of all I want to thank my family and parents. Their support have been the most important driving force in my life. I would never have been able to come this far without their love.

This research was graciously supported by the Army Research Laboratory STTR Grant W911NF-10-C-0002.

Table of Contents

LIST OF TABLES.....	IX
LIST OF FIGURES.....	X
CHAPTER 1: BACKGROUND	1
1.1 INTRODUCTION	1
1.1.1 THE FLAME IONIZATION DETECTOR	1
1.1.2 THE RESPONSE MECHANISM OF THE FID	4
1.2 REVIEW OF THE STATE OF THE ART	5
1.2.1 MICRO-COMBUSTION.....	5
1.2.2 PREVIOUS MICRO-FID WORK	6
1.3 GOAL AND OBJECTIVES	8
CHAPTER 2: MICRO-FLAME PHENOMENOLOGY AND ANALYSIS.....	11
2.1 EXPERIMENTAL SETUP FOR FLAME OBSERVATION	11
2.2 SILICON CHANNEL FABRICATION	13
2.3 RESULTS AND DISCUSSION	14
2.4 DETERMINATION OF OPTIMAL CHANNEL ANGLE BETWEEN AIR FLOW AND HYDROGEN FLOW USING FLUENT SIMULATION	17
CHAPTER 3: MICRO-FID CONFIGURATION	26
3.1 ELECTRODE FOULING.....	26
3.2 DESIGN	27
3.3 ELECTRODE FABRICATION.....	31
3.4 EXPERIMENTAL SETUP.....	32
3.5 RESULTS AND DISCUSSION	35
CHAPTER 4: SIGNAL STRENGTH ENHANCEMENT	39
4.1 THE NEED FOR ENHANCED SIGNALS	39

4.2 FLAME OBSERVATION	40
4.3 DESIGN AND MODIFICATION.....	42
4.4 EXPERIMENTAL SETUP.....	47
4.5 RESULTS AND DISCUSSION	48
CHAPTER 5: NOISE REDUCTION.....	53
5.1 FUNDAMENTAL CONSIDERATIONS.....	53
5.2 FABRICATION.....	57
5.3 RESULTS AND DISCUSSION	58
CHAPTER 6: DETERMINATION OF OPTIMAL OPERATIONAL CONDITIONS	64
6.1 OPTIMIZATION OF THE OXYGEN/HYDROGEN MASS FLOW RATIO	64
6.2 DETERMINATION OF MINIMUM SATURATION VOLTAGE.....	71
CHAPTER 7: SUMMARY, CONCLUSIONS, AND RECOMMENDATIONS FOR FUTURE WORK	73
7.1 SUMMARY AND CONCLUSIONS	73
7.2 OUTLOOK AND FUTURE WORK.....	78
APPENDIX A.....	80
A.1 SILICON CHANNEL FABRICATION.....	80
A.1.1 PATTERNING.....	80
A.1.2 ETCHING-ICP-DRIE (Inductively Coupled Plasma-Deep Reactive Ion Etcher)	82
APPENDIX B.....	83
B.1 ELECTRODE FABRICATION	83
APPENDIX C.....	84
C.1 SILICON CHANNEL FABRICATION (FLAME FOLDED FLAME)	84
C.1.1 PATTERNING.....	84
C.1.2 ETCHING-STP PEGASUS DRIE (Deep Reactive Ion Etcher).....	86
C.1.3 CLEANING	87
C.1.3.1 CLEANING (Piranha).....	87

C.1.3.2 CLEANING (SC-1).....	87
C.1.4 GROWING THERMAL OXIDE LAYER (ELECTRICAL INSULATION LAYER).....	88
REFERENCES	89

List of Tables

Table 2.1	The flame strain rate calculated for each channel design based on the simulation model.....	24
Table 3.1	Testing of Fig. 3.8 is repeated four times and each peak area is calculated and listed above. The average area of the peak is about 1.2 and 39.5 nC for the counter-flow flame design and folded flame design respectively. This implies that for 0.045 ml of injected methane at 3 atm (45 psi) in room temperature, the peak area was about 34 times larger for the folded flame design	37
Table 3.2	Micro-FID sensitivity as calculated by dividing each peak area with the injected amount of gram-carbons of 0.045 ml of methane.	37
Table 4.1	Flame structures obtained with the channel configuration of Fig. 2.3-(c). Channel (shown with arrows in the top-left panel) sizes were reduced about 60% in width, in order to reduce the fuel supported by hydrogen and oxygen supplied by a portable electrolyzer.	41
Table 4.2	Signal strength during pentane injection. The table reports the peak area for each injection and the calculated sensitivity of the micro-FID using the narrower Macor channel.	50

List of Figures

Figure 1.1.	Schematic diagram of a conventional flame ionization detector.....	2
Figure 2.1.	(a) Components of the micro-burner including two high temperature gaskets, two quartz plates, and a silicon channel. (b) The sandwiched assembly of the burner stack and the aluminum package. (c) The micro-burner stack was put into the square pocket of the aluminum package. (d) The final assembly of the aluminum package.....	12
Figure 2.2	Fabrication procedure of the silicon channels for flame observation.....	13
Figure 2.3	(a) Encapsulated flame structure when air and hydrogen channels met at a 90 ° angle. (b) Encapsulated counter-flow flame (i.e. streams meeting at 180 ° angle). (c) Flame with channel meeting at a 150 ° angle. Zoomed images show possible analyte loss for each design.....	15
Figure 2.4	The computed results of OH mass fraction on the left, actual image of OH chemiluminescence acquired with the intensified CCD camera on the right, both indicating the folded flame structure.	20
Figure 2.5	Starting from left to right each channel represent the flame simulation of 90 °, 150 °, and 180 ° respectively. As shown in the picture as well as in the simulation model, two distinct flames were observed in a 90 ° angle channel while 150 ° and 180 ° angle channels produced a connected flame.....	21

Figure 2.6	Simulation results of mass fraction of OH. Two distinct flames were observed until the channel met with an angle around 150°.....	19
Figure 2.7	Simulation results of velocity profiles for each channel design. These velocity profiles were used to calculate the flame strain rate for each channel design.....	21
Figure 3.1	Melted electrodes due to the high temperature of the flame. (a) The folded flame design produced a larger melting area with the shape of the foot print of the flame. (b) The counter-flow flame design produced a smaller melting area compared to the folded flame design. (c) An actual picture showing the relative position of flame and electrodes.....	28
Figure 3.2	Macor channel with the counter-flow channel configuration on the left (a) and the folded flame Macor channel on the right (b).....	29
Figure 3.3	Schematic of the micro-FID stack including the quartz-Macor-quartz sandwich structure (left) and an actual picture of the micro-FID stack including the high temperature silicone sealing gaskets (right).....	31
Figure 3.4	Schematic of the fabrication procedure for the Cr/Au electrodes on the quartz plate.....	32
Figure 3.5	A Vespel package where the FID stack is assembled with bar fittings for tubing and supplying the gases. The Vespel package also has holes for pogo	

	pins to serve as electrical contacts.....	33
Figure 3.6	Noise comparisons between the aluminum package and the modified Vespel package. The noise was reduced by 73 times. (3.6 V → 0.05 V).....	34
Figure 3.7	Schematic of the experimental setup, including air, hydrogen, methane gas tanks, injection system, electrical power supply, and signal detection devices.....	33
Figure 3.8	Two response signals from a folded flame (solid) and from a counter flow flame (dotted). These plots show the signal of the micro-FID over time when a sample gas of 0.045 ml of methane gas was injected. The flame was sustained with 120 ml/min of air and 80 ml/min of hydrogen. The picoammeter gain was set to 10^7 with 100 V applied to the electrodes.....	37
Figure 4.1	Flame structures obtained with the channel configuration of Fig. 2.3-(c). Channel (shown with arrows in the top-left panel) sizes were reduced about 60% in width, in order to reduce the fuel supported by hydrogen and oxygen supplied by a portable electrolyzer.....	41
Figure 4.2	(a) Previous larger Macor channel (b) Modified smaller Macor channel.....	43
Figure 4.3	(a) Previous Macor channel with larger injection port (b) Modified Macor channel with smaller injection port.....	45
Figure 4.4	Anchoring effect on the flame at the exhaust area due to the sharp corners...	46
Figure 4.5	(a) Smaller Macor channel (b) Modified smaller Macor channel with anchor	

	points.....	47
Figure 4.6	A schematic of the overall Experimental Setup.....	49
Figure 4.7	Result of ion current measurements during pentane injection.....	50
Figure 4.8	Comparison between the reduced size injection port and the large injection port.....	52
Figure 4.9	Comparison between the channel designs with and without the anchor points. A flow rate of 11 ml/min of oxygen, 21 ml/min of hydrogen, and 35.5 ml/min of air was supplied. Hexane was injected using the GC with a carrier flow of 2 ml/min and an injection volume of 0.1 μ l with a split ratio of 20 to 1.....	53
Figure 5.1	Macor channel melting due to the high flame temperature. The melted region of the gold pads represents the flame profile which is shifted to one side.....	55
Figure 5.2	(a) Cross view of a silicon wafer with silicon oxide grown layer on the outside. (b) Cross view of a SOI wafer with silicon oxide grown. The SOI wafer provides better electrical insulation due to the additional silicon oxide insulation layer inside.	56
Figure 5.3	Side view of the SOI channel. An additional step was created inside the channel. Fabricating an additional step to the channels with smaller widths improved the electrical insulation along the side-walls.....	57

Figure 5.4	The Faraday cage build to shield the entire vespel package and the micro-FID inside. The Faraday cage included BNC connectors for electrical connections. The entire package was electrically grounded to a single ground with the amplifier and the circuit board.....	58
Figure 5.5	Two background signals with and without the Faraday cage both using the SOI channel.....	60
Figure 5.6	Noise reductions when a SOI channel was used versus the Macor channel. Both noises were tested with the Faraday cage.....	61
Figure 5.7	Determination of the minimum detection level for hexane injection.....	62
Figure 5.8	Spectrum of the 17 SMAC compounds. All 17 compounds including BTEX are clearly separated and detected.....	64
Figure 6.1	The plot shows the response signal of the ion current signal. Air was varied from 22 ml/min to 45 ml/min and hydrogen flow was varied from 25.9 ml/min to 34.5 ml/min. Each data represents the average signal height of three repeated benzene gas injection of 0.01 μ l.....	67
Figure 6.2	The plot shows the response noise signal for each flow conditions. Air was varied from 22 ml/min to 45 ml/min and hydrogen flow was varied from 25.9 ml/min to 34.5 ml/min.....	68
Figure 6.3	The plot shows the signal to noise ratio for each flow conditions. Air was varied from 22 ml/min to 45 ml/min and hydrogen flow was varied from	

	25.9 ml/min to 34.5 ml/min.....	69
Figure 6.4	The plot shows the peak area which represents the collected ion current of the micro-FID. Air was varied from 22 ml/min to 45 ml/min and hydrogen flow was varied from 25.9 ml/min to 34.5 ml/min.....	70
Figure 6.5	The plot shows the response signal in volt11age of the injection peaks as the applied voltage is increased from 0 to 150V.....	73

Chapter 1: Background

1.1 Introduction

1.1.1 The Flame Ionization Detector

Since it was introduced in 1958 [1], the Flame Ionization Detector (FID) has evolved to one of the most commonly used tools of analytic chemistry. By far, the FID is the most commonly used detector in Gas Chromatography (GC) due to its wide dynamic range (on the order of 10^7) and its high sensitivity which is determined in terms of detected ion charge per gram carbon and is on the order of 0.015 C/gC [2-4]. Also the FID has a low Minimum Detection Limit (MDL - defined as a signal measured with a signal-to-noise ratio (S/N) equal to two), typically on the order of 1×10^{-10} gram carbon per second (gC/s) [5-7]. FIDs are commonly used for the quantification of volatile organic compounds in gaseous samples due to their high selective sensitivity to hydrocarbons. FIDs can be used as stand-alone devices for total hydrocarbon analysis (THA) or as detectors for GCs [6].

A schematic of a conventional FID is presented in Fig. 1.1. The FID is usually made of stainless steel and stainless steel fittings connect the detector to the appropriate gas supplies. The detector usually is connected with three separate gas supplies together with their respective mass flow controllers. The gases used for combustion are hydrogen and air (oxygen) while helium, nitrogen, and (less frequently) hydrogen gases are typically used as carrier gases. The carrier gas transports the samples through the column and delivers analytes to the flame that constitutes the “heart” of the device. The FID is

usually placed in a separated oven to ensure that no solutes are condensing in the connection tubes and columns [4].

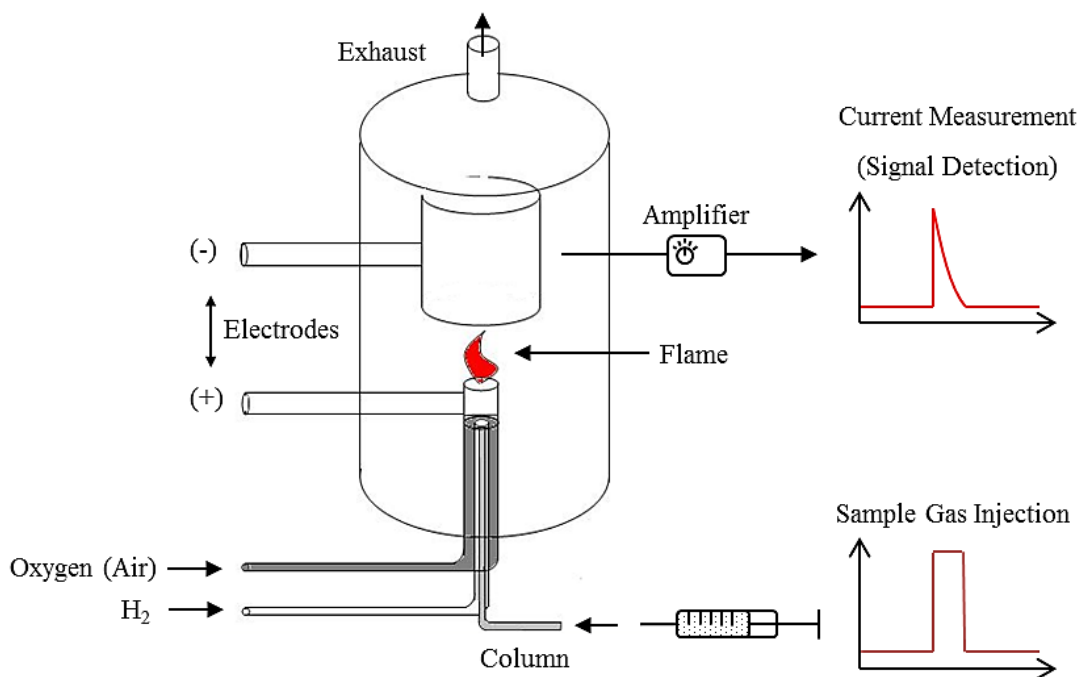


Figure 1.1 Schematic diagram of a conventional flame ionization detector.

As shown in Fig. 1.1, two electrodes are used to apply an electric field around the oxy-hydrogen flame to collect the ions produced. Generally, one electrode is the burner itself and the second electrode surrounds the oxy-hydrogen flame [8]. The measurement is operated in a saturated voltage mode that ensures the collection of all charges formed [9]. Consequently, the FID measures the ion current produced during ion collection. This current correlates with the amount of carbon in a flame through a mechanism that is described in detail below. In order to measure the small ion current, an amplifier

amplifies the signal and sends it to a data acquisition device. The final output depends on the software, but in general a graph is displayed with the time on the x-axis and the ion current on the y-axis.

High-temperature electric insulators are selected to insulate the jet and the electrodes from the main body. Material selection is critical as many ceramics and glasses become conducting at high temperatures (200-300 °C) [4]. The use of the high voltage to create the electric field in conjunction with the relatively small ion current requires a well-insulated structure and material selection. In order to accommodate the high temperature produced from the oxy-hydrogen flame and the operation in an oven, the insulating materials need to be thermally stable. Thus, the tip of the burner is usually constructed of metals such as stainless steel, platinum or platinum/rhodium alloys.

For the injection of the analytes the FID is usually connected to the end of a GC. The GC is used for chemical analysis that separates chemical mixtures into their components through selective adsorption of its compounds during its passage through a coated narrow tube (column). The coating known as the stationary phase separates the different components of the mixture, causing each component to exit the column at a different time. Detectors such as an FID are usually connected to the end of the column for the detection of the analytes.

1.1.2 The response mechanism of the FID

It was early discovered during a study of a Bunsen burner flame that the electric conductivity of the internal cone was about 100 times higher than the outer region of the flame [4]. Also, it was reported that the lower part of the Bunsen burner flame contained more ions than the upper radiating region of the flame. The presence of the ions could not be explained through a thermionization process. For this reason, the concept of chemionization was introduced in 1955. By chemionization, we mean series of reactions between electrically neutral molecules and/or radicals that generate electrically charged ions as products [4, 10, 11].

The working principle of the FID depends on the fact that an oxy-hydrogen flame produces relatively few ions (10^7 ions/cm³), while the number of ions increases through addition of hydrocarbons (10^{10} ions/cm³) [10]. The generally accepted explanation is that ions are not formed by thermal ionization but by thermal emission from microscopic carbon particles that are formed during the combustion process. In other words, the oxy-hydrogen flame releases the thermal energy which splits the organic compound into radicals that react with oxygen and produce a large amount of ions. Then the formylium ion (CHO^+) reacts rapidly with water to produce hydroxonium ions (H_3O^+), which are the primary charged ions responsible for FID response. The corresponding chemical reactions are as follows:



The yield of ions is known to be on the order of one per 10^6 carbon atoms [12-15]. The detector signal is proportional to the number of carbon atoms present in the sample gas. Thus, the FID is called a “carbon counting device”. On the other hand, inorganic substances, as well as already oxidized compounds such as carbon dioxide, cannot be detected by the FID since the ions are a result of chemical ionization of hydrocarbons [16].

1.2 Review of the State of the art

1.2.1 Micro-combustion

Until recently, the concept of a microburner was thought to be impossible. Early work by Davy [17] established the notion of the so-called “quenching diameter”, i.e. critical minimum hardware dimension (usually of the order of a few millimeters) below which no flame could be sustained. However, recent work showed that by careful material selection of the walls (that do not quench radicals so that the gas-phase combustion reactions can occur unimpeded) and thermal insulation, micro-combustion was possible. The field has developed mainly with the objective of portable, combustion-based power sources that would operate as “liquid-fuel batteries” and included combustor for anything from micro-gas-turbines to micro-Wankel and micro-Stirling engines [18-34]. Of particular importance to this work is the micro-combustor of [35-37] that was built with techniques of microscale manufacturing and utilized 35 mm long channels with a cross section of $5 \times 0.75 \text{ mm}^2$.

Micro-combustion for micro-thermal engines did not prove (for the most part) successful, mainly because of difficulties in separating the hot from the cold side of the thermal engine. However, analytical chemistry may be a more promising field of applications of micro-combustion. In particular, recent developments in micro-fabrication have initiated the field of micro-reactor engineering, which has impacted a virtual revolution in the technology of portable and MEMS-based devices for analytic chemistry. In terms of combustion technology, this brings up the exciting possibility of a “flame-on-the-chip” that could be used as the main element of portable micro-FIDs [38, 39]. Early efforts towards this goal [2-4] focused on the miniaturization of large-scale FIDs, which employed either premixed or non-premixed flames. Issues in hardware and thermal management were addressed as well. However the actual flame was not a micro-flame encased in the FID hardware, but perhaps a small, certainly non-micro, and candle-like flame which burnt freely, thus limiting severely the portability of the ensuing device. Early efforts in micro-combustion produced results that were not consistent with large-scale flame behavior and pointed to the existence of previously unknown combustion physics in small-scale devices. In particular, previous work from this group in [40] revealed intriguing instabilities in non-premixed flames in sub-millimeter silicon channels, which to our knowledge have not been fully explained theoretically yet [41].

1.2.2 Previous Micro-FID work

Increasing interest in miniaturization and portability has led to the development of portable GCs (micro-GCs) [42-46]. A portable FID compatible with a portable GC is an

attractive analytical instrument because it can be used to identify chemical threats, spills, and perform environmental monitoring on site. Low gas consumption, small size, and low power requirements for operation and heating are additional benefits obtained from a miniaturized FID (micro-FID).

To date, a few miniaturized FIDs have been proposed. Stable flames are difficult to sustain at a small scale due to their enhanced heat loss that is caused by the large surface-to-volume ratio, while catalytic combustion can sustain a flame with a relatively low fuel consumption rate. A micro-catalytic combustor was made up of a catalytic film deposited on the surface of a micro-scale hot plate [3, 10]. However, the presence of catalysts affects the generation of ions from hydrocarbons, which then reduces the FID signal. This makes application of catalytic combustion challenging for micro-FIDs.

Kuipers and Müller [7, 8, 14] proposed a micro-FID using a premixed oxy-hydrogen flame. However, a premixed flame is hard to control with respect to flame position and flame shape. On the other hand, combustion in a diffusion flame occurs in a thin flame sheet where fuel and oxidizer meet at stoichiometric proportion. The gas velocities are small at this location and heat loss due to convection is relatively small. This makes the flame position and shape relatively easier to control in diffusion flames than in premixed flames [8, 47]. The residence time of the fuel and the analytes in the combustion zone is relatively long, which produces a stable flame and higher ion yield and makes a diffusion flame more suitable for the development of a micro-FID.

In conventional, large-scale FIDs, both premixed and diffusion flames have been used that are not encapsulated but are rather open to the environment [10]. In order to

prevent the system from environmental contamination, excessive airflow was used to shield the system [7]. To avoid any excessive use of air Zimmermann et al. [2, 15] proposed an encapsulated glass-silicon-glass sandwich structure. This sandwich structure was efficient respect to shielding the flame inside from the environment. However the use of glass (or pyrex) can result in leakage current and drifting signals. Thus we propose to develop a micro-FID using quartz instead of pyrex, which can reduce the leakage current even at increased temperatures of operation. In closure, although the concept of a micro-FID has been proposed before, the device-level attempts so far have been mostly empirical proofs of concept that have not harnessed the fundamentals of combustion science and micro-fabrication technology. This is a gap that this thesis aspires to cover.

1.3 Goal and Objectives

Building on this earlier work, we present the fundamental phenomenology of encapsulated, non-premixed, micro-FID flames. These flames will operate with residence times, which will detect gas analytes with minimal loss and, moreover, consume smaller hydrogen flow rates than the ones employed for open flames. In this manner, a portable micro-FID device can be powered with a typical small-size battery that will electrolyze small amounts of water (on the order of a few cc per hour). Additional work is concerned with the influence of operating parameters on the sensitivity of the micro-FID. The influence of hydrogen, oxygen flow, saturation voltage, as well as sample concentration on the device performance will be examined. Whenever

relevant, the results will be supported by flame visualization. In addition, the research focuses on analyzing the minimum detection limit (MDL) of the device by determining and minimizing the noise signals.

The overarching goal of this thesis is to develop a micro-FID using a diffusion flame which can be operated with low enough oxy-hydrogen gas consumption so that it can be operated through electrolysis with a portable battery. Using electrolysis for producing hydrogen has benefits over other methods since water can be carried around for portable applications. The scientific and technological fundamentals are established that will allow portable, agile, combustion-based gas analysis. The work will provide sensitivity and selectivity that is comparable to conventional macro-scale FIDs with lower oxygen and hydrogen consumption. Therefore, the work will focus on enhancing signal strength and reducing noise level. In order to achieve the overarching goal, the following specific objectives will be pursued:

- A micro-burner will be designed with different configurations of silicon channels and tested in order to create an air-hydrogen diffusion flame that can be sustained in small silicon enclosures with as small flow rates as possible. The miniaturized diffusion flame will be evaluated in order to find the optimal silicon channel configuration in terms of strength of the FID signal.
- The effect of channel geometry on flame structure will be explored with a commercially available CFD code. Flame shape for each channel configuration will be determined and the flame strain will be calculated to verify the stability of the flame.

- A prototypical micro-FID will be constructed in order to test different channel designs. The response ion current will be measured to determine the desired channel design for further development of the micro-FID.
- Micro-FID performance will be measured and optimized through reducing the overall fuel consumption and increasing the detection sensitivity in order to obtain a high signal-to-noise ratio.
- Particular emphasis will be placed on noise reduction, which is of course connected to achieving a low detection limit and a high signal-to-noise-ratio.

Overall, the thesis contributes to micro-combustion science through establishment of micro-diffusion-flames in silicon enclosures. It also contributes to gas-analysis technology through the establishment of a portable micro-FID that can operate using a hydrogen-oxygen flame fueled by mass flow rates generated through water electrolysis with a small portable battery.

Chapter 2: Micro-Flame Phenomenology and Analysis

2.1 Experimental Setup for Flame Observation

In order to obtain the “flame-on-the-chip”, we configured the micro-burner of Fig. 2.1. Micro-burner components include a high-temperature silicone gasket, a quartz plate (1 in \times 1 in \times 0.062 in, Technical Glass Products, Painsville, OH, U.S.), the silicon channel in which the flame was stabilized, another quartz plate, and finally another high temperature gasket. These components were assembled in a manner that created an encapsulated quartz-silicon-quartz sandwich structure. This particular sandwich structure prevented the flame from being exposed to the environment. This stack was encased in an aluminum package that included holes to introduce the air and hydrogen gas into the stack (Fig. 2.1-(b)). The aluminum package was designed with a small square pocket for the micro-burner stack as shown in Fig. 2.1-(c). Figure 2.1-(d) presents the assembled package. The aluminum package had a fluidic connection on the outside to provide air and hydrogen through 1/8" tubing. During experimentation, air and hydrogen flows were metered with FMA 5400/5500 mass flow controllers of Omega Inc.

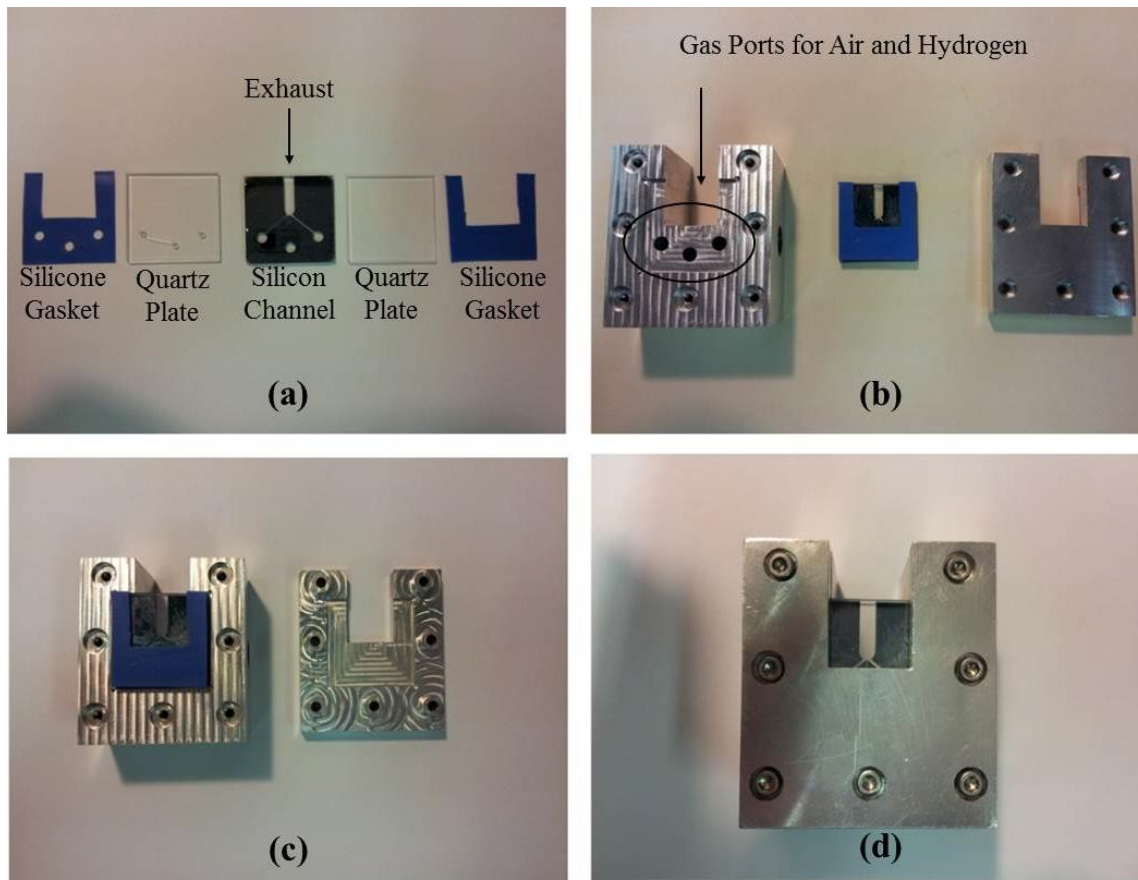


Figure 2.1 (a) Components of the micro-burner including two high temperature silicone gaskets, two quartz plates, and a silicon channel. (b) The sandwiched assembly of the burner stack and the aluminum package. (c) The micro-burner stack was put into the square pocket of the aluminum package. (d) The final assembly of the aluminum package.

2.2 Silicon Channel Fabrication

The silicon channels were fabricated using 750 μm thick (100) silicon wafers. The wafer was first spin-coated with AZ4620 photo resist (PR). Then the wafer was baked at 60 $^{\circ}\text{C}$ for 2 minutes and at 110 $^{\circ}\text{C}$ for another 2 minutes. This step is called soft-baking which reduces the remaining solvent and built-in stresses [48]. This step prevents the wafer from sticking to the mask during the exposure step. The wafer was exposed to ultraviolet (UV) light using the mask aligner. After exposure, the entire wafer was developed in a solution mixture of AZ 400 K developer and deionized (DI) water mixed with a ratio of 1:4 (developer: DI water) for about 2 minutes. The wafer was then quenched in DI water and dried with the nitrogen gun. The wafer was through etched with an inductively coupled plasma-deep reactive ion etcher (ICP-DRIE). Once the silicon channel was etched, the wafer was dipped into the 400T PR stripper to remove the remaining PR. (A step by step fabrication step is provided in the Appendix A)

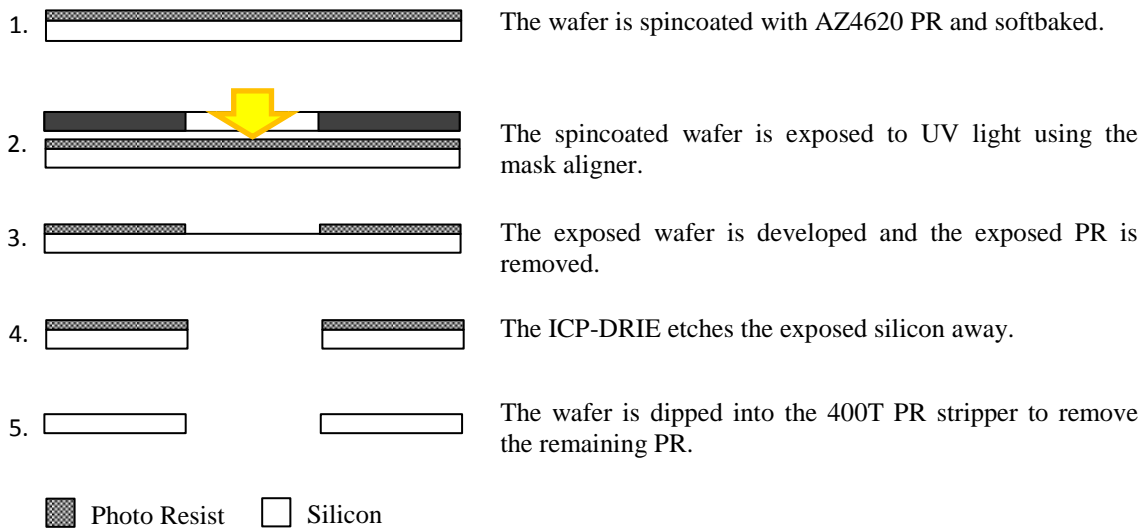


Figure 2.2 Fabrication procedure of the silicon channels for flame observation.

2.3 Results and Discussion

Flames were ignited by holding a lighter close to the exhaust hole of the micro-burner. The location of the exhaust hole can be observed in Figs. 2.1 and 2.3. The flame was first established at the exhaust area and then guided into the channel by adjusting the flow rate of the fuel. Initial ignition took longer while the later ignition happened faster once the package was heated up. The flame speed was faster for the higher wall temperature and thus the increased package temperature helped the flame propagate into the channel.

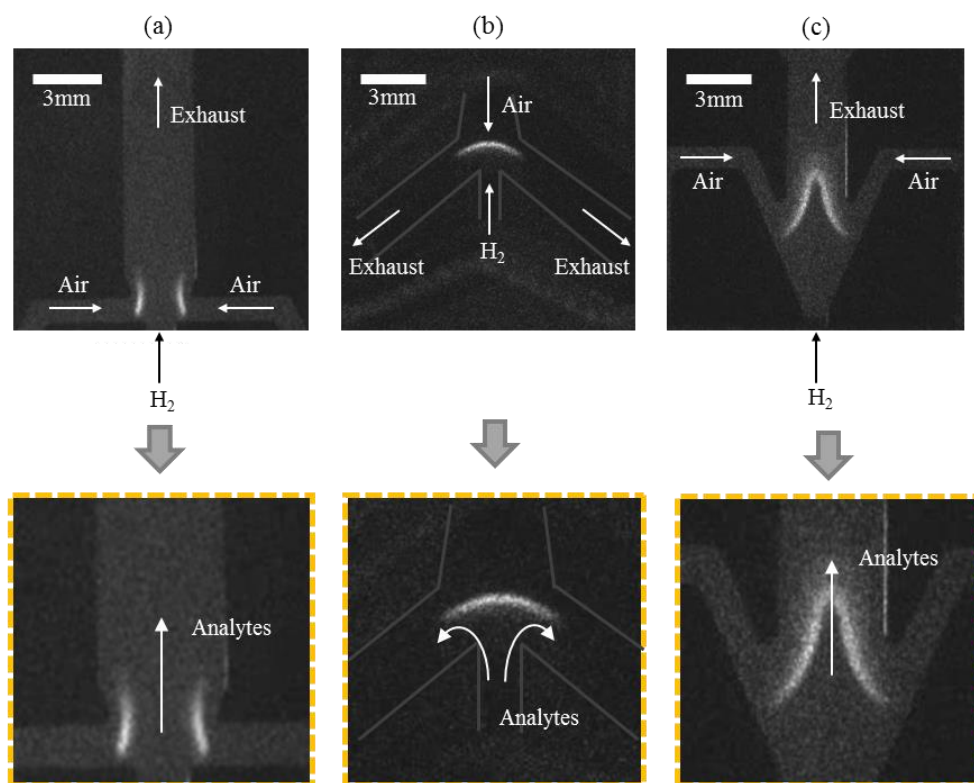


Figure 2.3 (a) Encapsulated flame structure when air and hydrogen channels met at a 90° angle. (b) Encapsulated counter-flow flame (i.e. streams meeting at 180° angle). (c) Flame with channel meeting at a 150° angle. Zoomed images show possible analyte loss for each design [49].

Figure 2.3-(a) shows a representative image of a flame taken with an ICCD camera. This flame structure was obtained when the air and hydrogen channel met at a 90 ° angle to each other. The image was taken when the flow rates of air and hydrogen were 40 ml/min and 80 ml/min respectively. As shown in Fig. 2.3, two distinct flames were observed at the left and right side of the channel. This was probably due to the extinction of each of the two flames because of high strain. In fact, the applied flow rate corresponded to a speed of the air stream equal to 0.44 m/s and hydrogen stream of 1.78 m/s. The Reynolds numbers were 14 and 2 for the air stream and hydrogen stream respectively with physical properties of the gases calculated at 300 °C. The strain imposed on the flame was estimated using the following equation as suggested in [50] as equal to 746 s⁻¹.

$$K = \left(\frac{du}{dx}\right)_{flame} = \frac{2U_{ox}}{L} \left[1 + \frac{U_{fuel}}{U_{ox}} \left(\frac{\rho_{fuel}}{\rho_{ox}}\right)\right]^{1/2} \quad (1)$$

This was a very high strain rate (as compared e.g. with the ones typically reported in [17]) and causes the double extinction shown in Fig. 2.3-(a). This flame structure could lead to loss of analytes due to the possible leak between the two distinct flames as indicated with the arrows passing the flame in Fig. 2.3-(a). Thus, this channel configuration leads to a potential loss in the signal for the micro-FID.

Figure 2.3-(b) shows the flame shape obtained with the second design, which was the counter-flow channel design. In this design, air came from the top to meet the hydrogen that came from the bottom. The volumetric flow rate was 80 ml/min for both the air and hydrogen. This corresponded to a speed of the air stream equal to 1.78 m/s

and hydrogen stream of 3.6 m/s. The Reynolds numbers were 223 and 19 for the air stream and hydrogen stream respectively with physical properties of the gases calculated at 300 °C. The strain imposed on the flame was estimated to 673 s^{-1} . However this counter-flow flame design shown in Fig. 2.3-(b) still loses analytes around the exhaust channels where the tails of the flame are extended indicated in Fig. 2.3-(b). Part of the sample analytes could leak along the channel without being ionized.

When air and hydrogen streams met at a 150° angle, a stable single folded flame was observed as shown in Fig. 2.3-(c). This flame structure was obtained by applying air and hydrogen with the same flow rate of 80 ml/min from the side and bottom, respectively. This corresponded to a speed of the air stream equal to 0.44 m/s and of the hydrogen stream equal to 0.59 m/s. The Reynolds numbers were 223 and 19 for the air stream and hydrogen stream respectively and the strain imposed on the flame was estimated at 162 s^{-1} , i.e. substantially smaller than the one of both the 90° and the counter-flow configuration. This allowed for a vigorous hydrogen-air encapsulated flame that minimized analyte leakage and could be used for high accuracy, micro-FID detection of analytes.

2.4 Determination of Optimal Channel Angle between Air Flow and Hydrogen Flow Using FLUENT Simulation

It has already been shown experimentally in the previous sections that different channel angles provide different flame shapes. However experiments can only provide a few data points on how different channel angles would affect the flame shape and position. Simulations on the other hand can explore the relation between channel angle and flame structure in detail and thus provide valuable information that can be used for channel design and improvement of micro-FID performance.

Such simulations were performed with a computational fluid dynamics (CFD) software package ANSYS FLUENT. The code is used in order to solve the continuity, momentum, energy and species equations. Non premixed flamelets are used for combustion modeling. Mixture fraction is used as the independent variable that controls flamelet structure. The mixture fraction, f , can be written in terms of elemental mass fraction as:

$$f = \frac{Z_k - Z_{k,O}}{Z_{k,F} - Z_{k,O}}$$

where, Z_k is the elemental mass fraction of some element k while the subscripts F and O denote fuel and oxidizer stream respectively. Clearly for the mixture at the air nozzle, the mixture fraction is equal to 0, whereas it is equal to 1 in the hydrogen stream. The flame sits in the mixing layer at the location where the mixture fraction has a value equal to the stoichiometric one.

The FLUENT software provides a built-in tool that was used to design different channel designs and generate the computational grids. Using this software tool, two-dimensional structures were designed in which the channel angle varied between 90° to 180° with a 10° interval. The channel width was specified and set equal to $1000\ \mu\text{m}$ for the air flow channels and $1600\ \mu\text{m}$ for the hydrogen flow channels, based on the dimensions of the actual silicon channels introduced in the previous chapters.

After the channels were designed the ANSYS FLUENT meshed the designed structure in order to assign cells, faces, and grid points. Once the structure was built, the governing equations for the non-premixed flame were coupled with a model of oxidation kinetics that included 10 species, namely O_3 , O , HONO , HO_2 , H_2O_2 , OH , H_2O , H , O_2 , N_2 , and H_2 . Temperature measurements of the exhaust gas were taken by inserting the tip of a thermocouple into the exhaust and used as boundary conditions. For wall temperature boundary conditions, published results of [51] were used for this configuration. The simulation was run for the case of hydrogen and air inlet velocities of $1.6\ \text{m/s}$ and $0.5\ \text{m/s}$ respectively, and the inlet temperatures of $300\ \text{K}$.

The initial goal of the computational effort was to compute results that could be compared with the experimental results of section 2.3. The flame pictures in Fig. 2.3 were obtained using an intensified charged coupled device (CCD) camera and record OH chemiluminescence for the hydrogen-oxygen flame. The result of Fig. 2.4 shows the computed results of OH mass fraction on the left, and actual image of OH chemiluminescence acquired with the intensified CCD camera on the right, both indicating the folded flame structure.

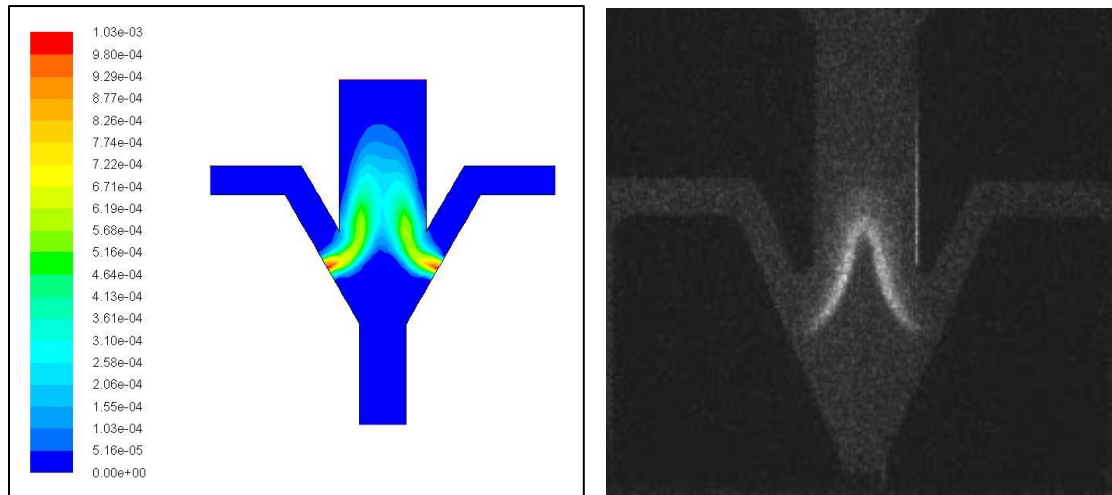


Figure 2.4 The computed results of OH mass fraction on the left, actual image of OH chemiluminescence acquired with the intensified CCD camera on the right, both indicating the folded flame structure.

The simulation results captured the flame structure recorded during the experiments. In particular, the computational results demonstrated the folded flame structure which was observed with the ICCD camera. Based on this result, channels with different angles between the air and hydrogen stream were created. The following result in Fig. 2.5 shows the three channel designs that were introduced in section 2.2.

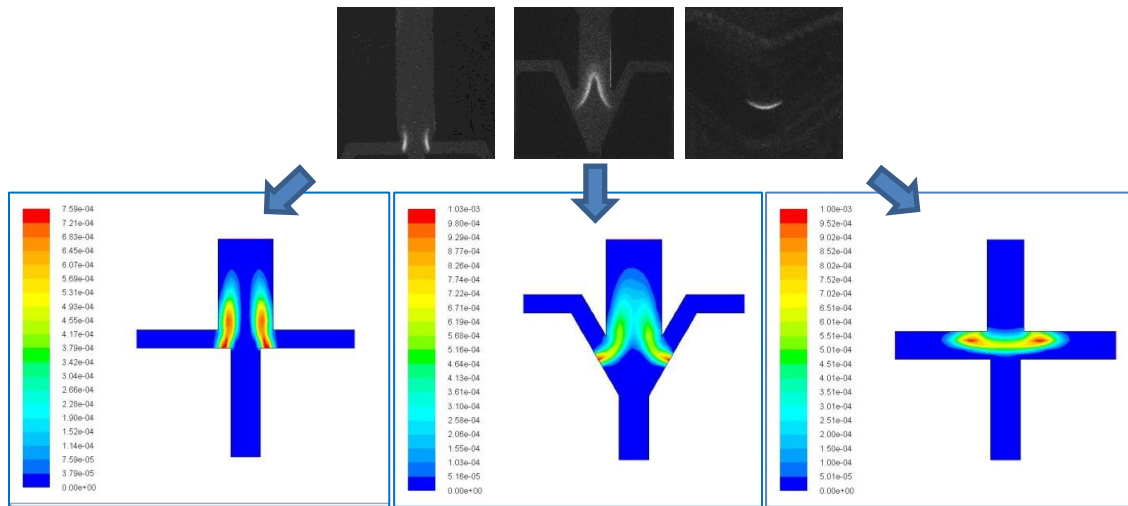


Figure 2.5 Starting from left to right each channel represent the flame simulation of 90° , 150° , and 180° respectively. As shown in the picture as well as in the simulation model, two distinct flames were observed in a 90° angle channel while 150° and 180° angle channels produced a connected flame.

In Fig. 2.5 starting from left to right each channel represent the flame simulation of 90° , 150° , and 180° respectively. As observed from the pictures taken by the intensified CCD camera, two distinct flames were observed with the 90° angle channel while the 150° and 180° angle channel produced a more connected flame. We considered this qualitative agreement a validation of the code in that the simulations could capture flame structure, which was the crucial feature of the design. E.g., the simulation result confirmed that the configuration whereby the two channels met at a 90° angle had the most chance of losing analytes through the gap between the two distinct flames.

A parametric study of flame structure is shown in Fig. 2.6. Channel designs were designed by increasing the angle with a 10° increment.

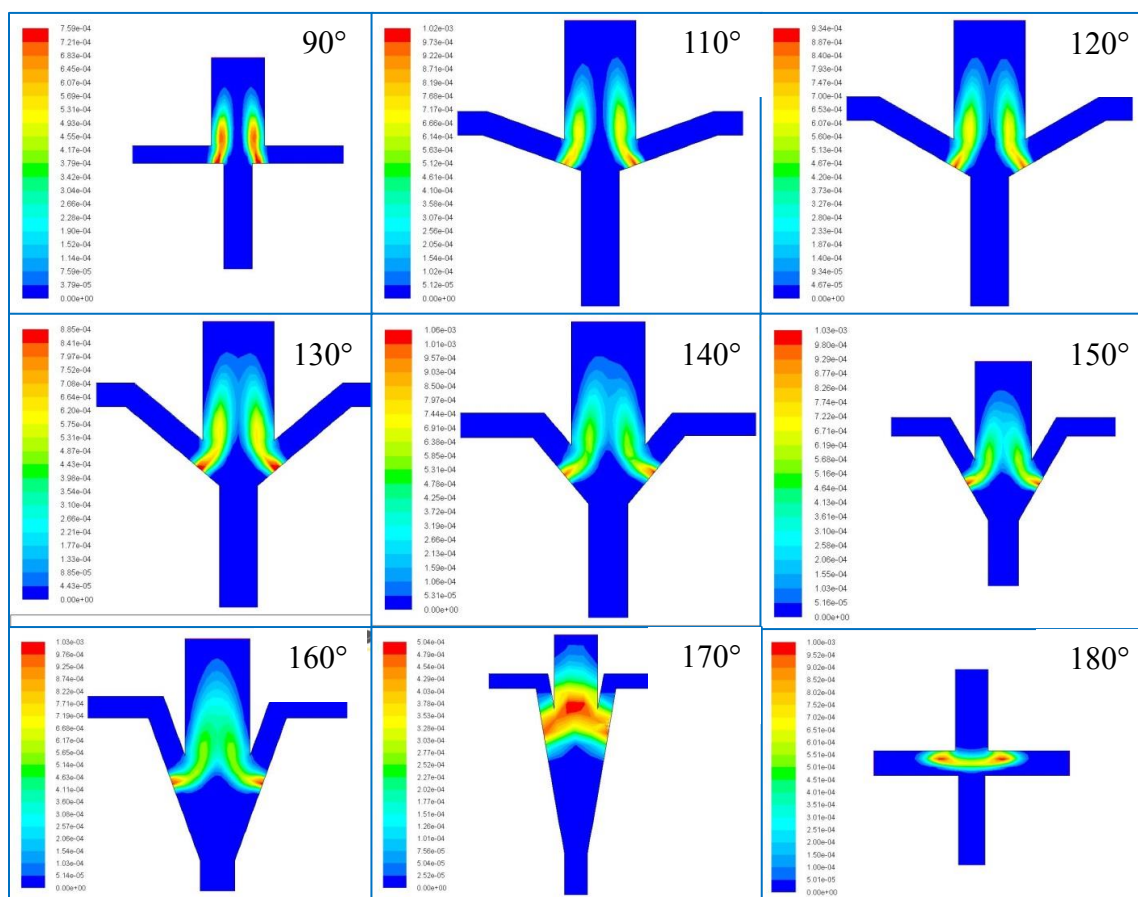


Figure 2.6 Simulation results of mass fraction of OH. Two distinct flames were observed until the channel met with an angle around 150° .

These results indicate the channel designs that cause minimal analyte loss. In particular, two distinct flame structures were generated when the channels guided the hydrogen and air flow with an angle between 90° to 140° . However, once the channel angle reached around 150° the flame profile started to create a single flame with a folded flame structure. Around 150° - 160° angle the channel configuration showed the most preferred flame structure. It can be determined from the simulation results that the 150°

and 160° channel provided a folded flame structure that could minimize the loss of analytes. This result suggests that the fabrication of channels with an angle between 150° to 160° is the most suitable for our micro-FID.

Also velocity field was computed in order to calculate the strain rate for each case. The results of velocity field calculations are shown in Fig. 2.7. The strain rate at the flame location for each channel configuration was calculated as follows. The flame was considered at the stabilization locations near the wall in Fig. 2.6. These are locations where the flame burns rigorously, even when it is not singly connected (i.e. in the cases where the angle of intersection of the channel axes is substantially less than 150°). There, a flame thickness can be estimated from the OH results of Fig. 2.6. If one divides the velocity jump across the flame with this flame thickness, an estimate of local strain on the flame can be acquired. Results of these calculations are shown in Table 2.1.

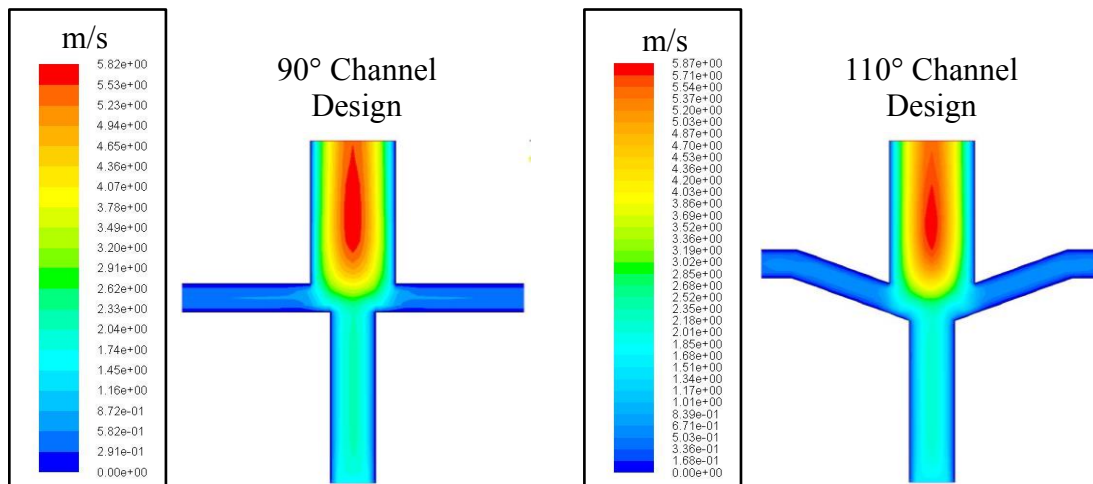


Figure 2.7 (Cont.)

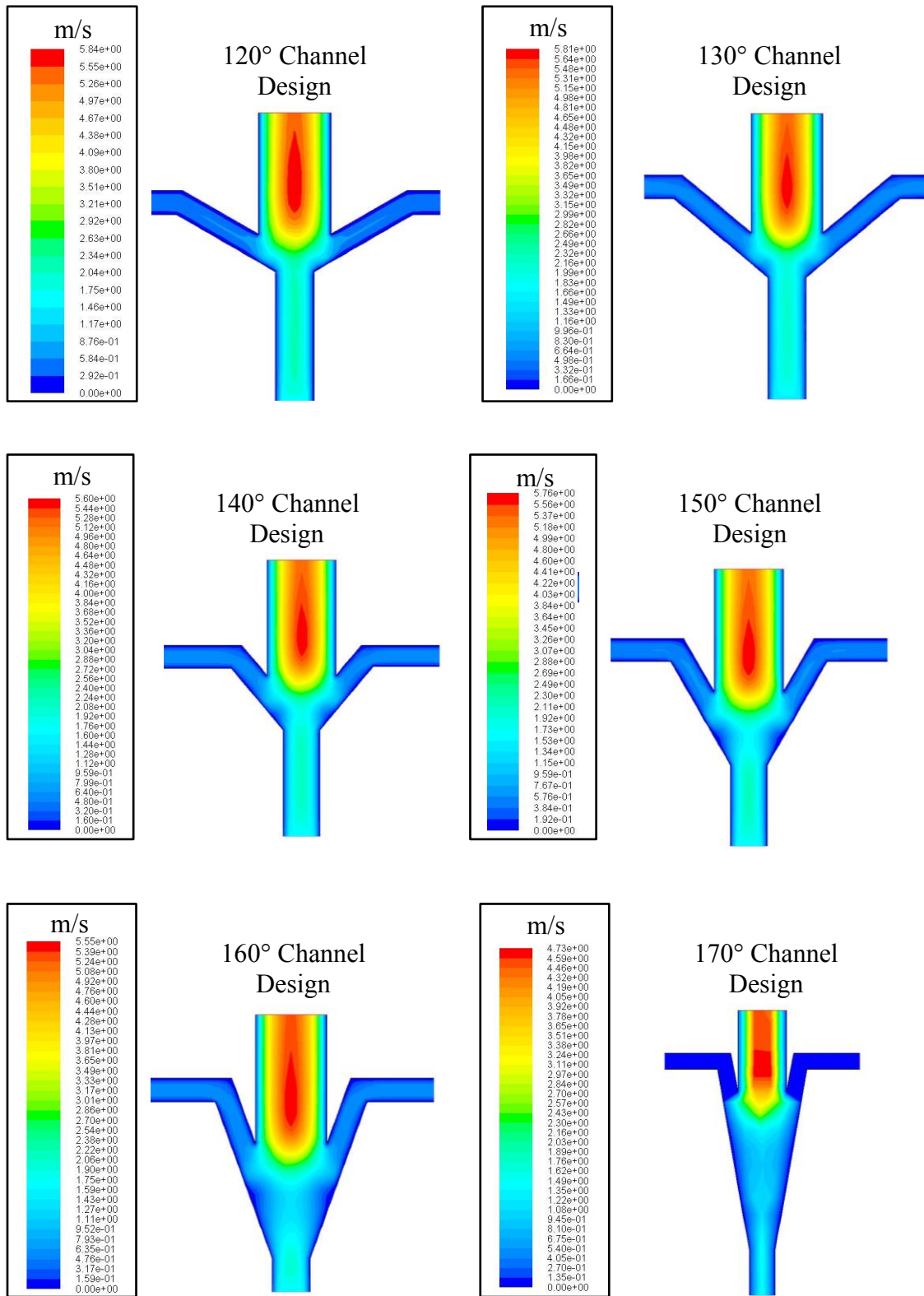


Figure 2.7 (Cont.)

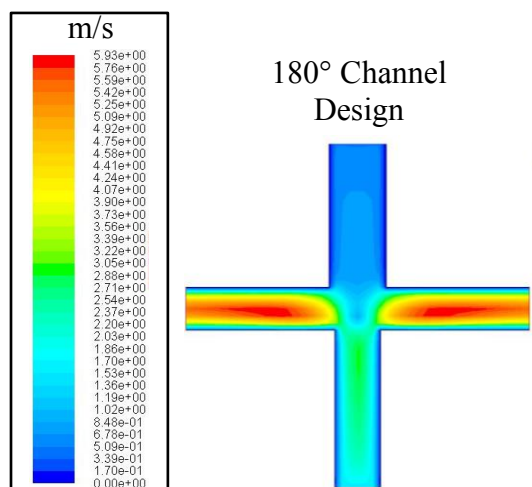


Figure 2.7 Simulation results of velocity profiles for each channel design. These velocity profiles were used to calculate the flame strain rate for each channel design.

The following Table 2.1 represents calculation results of the flame strain rate based on the simulation model.

Channel Design	Strain (1/s)
90 °channel design	3435
110 °channel design	2292
120 °channel design	1945
130 °channel design	1534
140 °channel design	1201
150 °channel design	962
160 °channel design	919
170 °channel design	542
180 °channel design	1580

Table 2.1 The flame strain rate calculated for each channel design based on the simulation model.

It can be determined from the calculated results shown in Table 2.1 that the flame strain reduces with an increasing channel angle between the air and hydrogen flow. Again, these results follow the tendency that was observed in the previous flame strain calculations that was obtained with the flame pictures. The 90° channel design produced highest strain rate and thus being most unstable among the channel designs. Channel designs with an angle around 150°-170° produced a relatively lower strain rate and providing a more stable flame structure. This result suggests that the fabrication of channels with an angle between 150° to 170° is suitable respect to the flame strain rate. In conclusion, it is suggested to design and fabricate the channel within the range of 150° to 160° to minimize the leakage of the analytes as well as to obtain a relatively low strain rate.

Chapter 3: Micro-FID Configuration

3.1 Electrode fouling

As discussed in the previous chapter, the proposed folded flame configuration (150° angle) has the advantage of operating with a lower flame strain rate and was more stable compared to the counter-flow flame design. In addition, the folded flame design provided a flame shape that could minimize the leakage of the analytes. However the folded flame produced a larger flame area which could melt a larger area of the electrode as shown in Fig. 3.1-(a). Melting of the gold electrode surface leads to unwanted drift and noise signals. On the other hand, as shown in Fig. 3.1-(b) the counter-flow channel design provided a flame shape that facilitated operation in the sense that it had a smaller flame area and thereby reduced the electrode damage. Thus the counter-flow channel design and the folded flame design were tested in order to compare performance with respect to the durability of electrodes and the possibility of leakage of the analytes. Electrodes were designed so that they were not exposed directly to the flame. A representative electrode design for a folded flame design is shown in Figs. 3.1 (a) and (c).

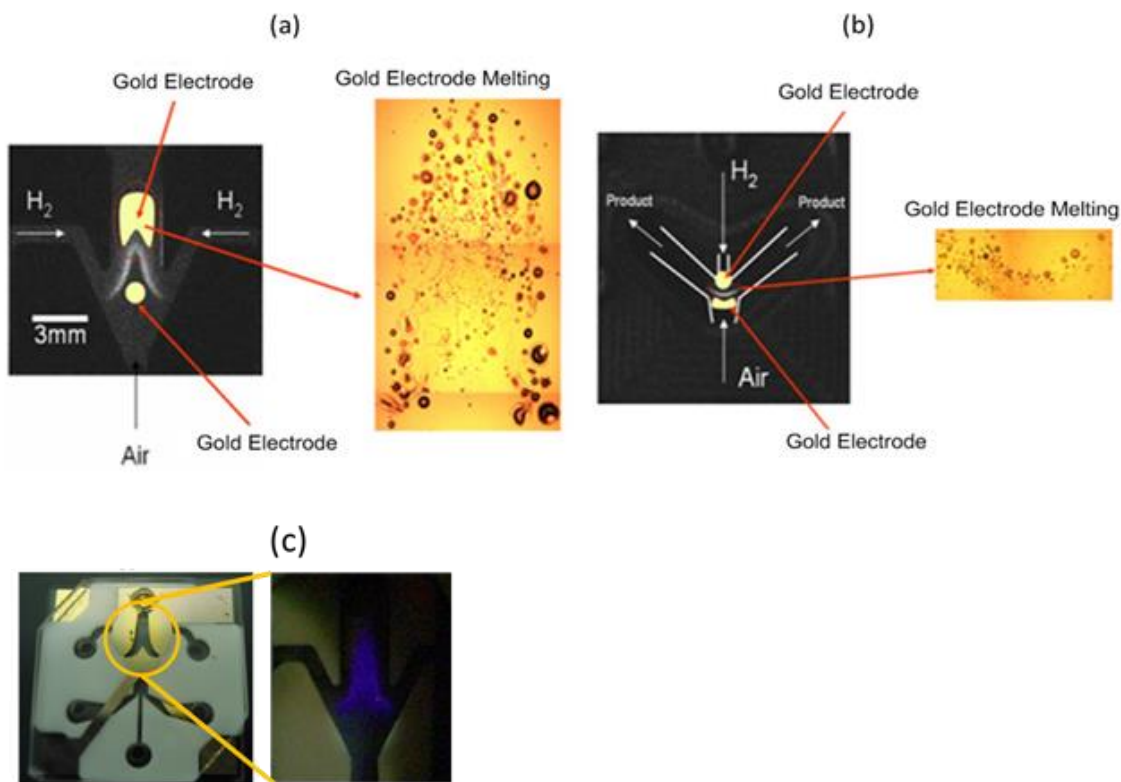


Figure 3.1 Melted electrodes due to the high temperature of the flame. (a) The folded flame design produced a larger melting area with the shape of the foot print of the flame. (b) The counter-flow flame design produced a smaller melting area compared to the folded flame design. (c) An actual picture showing the relative position of flame and electrodes [49].

3.2 Design

As shown in Figs 3.1-(a) and 3.1-(b), the melting area of the gold electrodes was localized along the flame region due to the high flame temperature. In order to avoid the melting of the electrodes and have the electrodes located as close as possible to the flame, electrodes were designed around the foot print of the flame and split into two parts which

were surrounding the top and bottom part of the flame as shown in Fig. 3.1-(c). This specific electrode design created an electric field close to the flame that measured the resultant ion current.

The basic design components of the micro-FID were similar to the micro-burner components introduced in section 2.1. Initially, silicon channels with an oxide insulation layer grown on top were proposed for the channel material of the micro-FID. However, the oxide layer was easily scratched during the assembly causing electrical short problems. Thus, the micro channels were machined with a 750 μm thick Macor substrate which is a glass ceramic with an exceptionally high electrical resistivity of 10^{16} $\Omega\text{-cm}$.

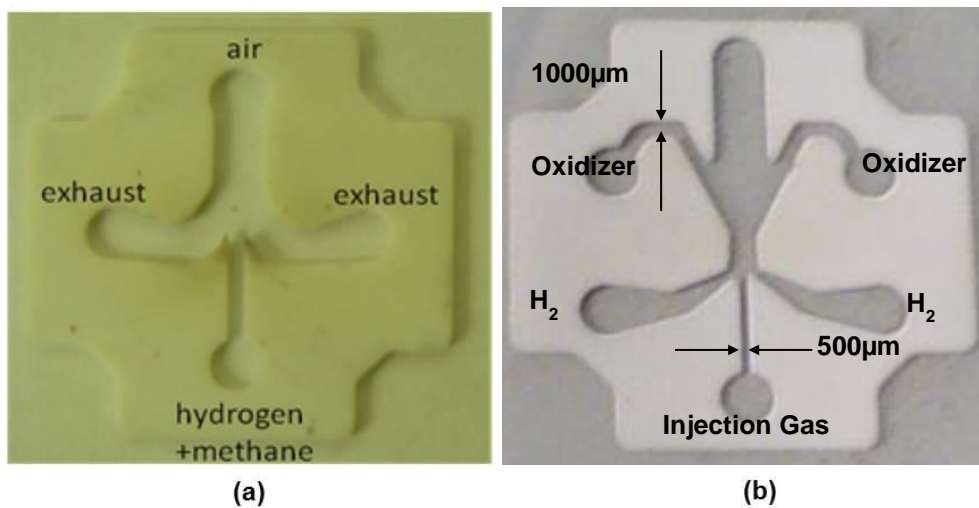


Figure 3.2 Macor channel with the counter-flow channel configuration on the left (a) and the folded flame Macor channel on the right (b)

Figure 3.2 shows the Macor channel of the counter-flow (a) channel and the folded flame channel (b). As indicated in Fig. 3.2-(a), using the counter-flow channel configuration, air and hydrogen gas was supplied from top and bottom respectively while the resulting exhaust gas was guided to both sides of the channel. The sample gas was injected into the hydrogen stream and guided to center of the channel where the flame sustained. Figure 3.2-(b) shows the folded flame Macor channel where the air was guided from the sides by both upper channels and hydrogen guided from the sides through the lower channels as indicated. Instead of mixing the injection sample gas with the hydrogen flow (as we did for the counter-flow channel), the folded flame channel included an independent injection channel. The additional channel, guiding the injection gas to the middle section of the channel (burner cavity) was integrated in order to reduce dead volume of the sample gas to generate a sharper peak. This additional injection port was also used to confine the injection gas and prevent broadening of the sample analytes during the injection.

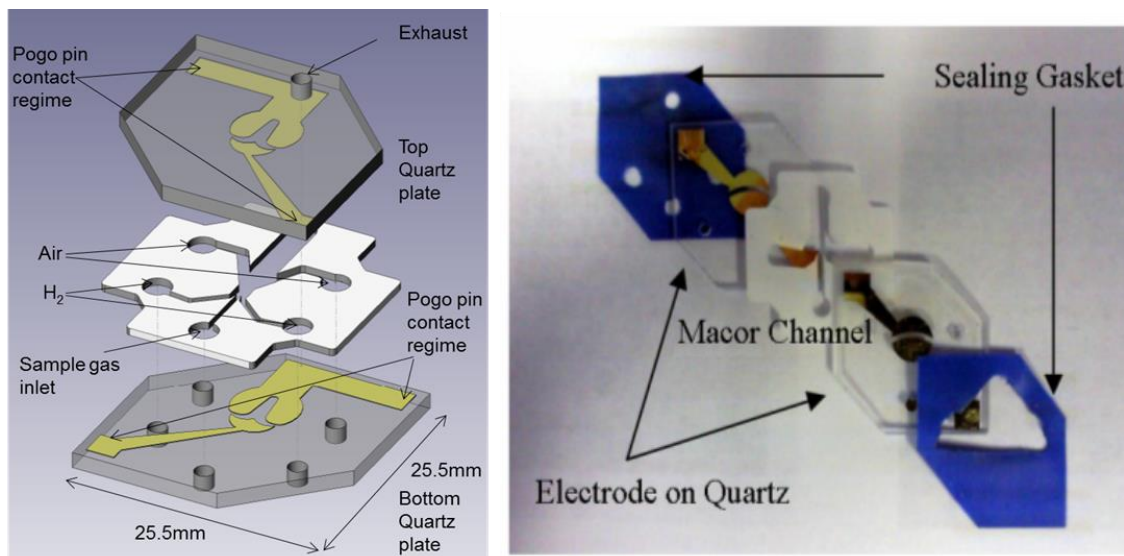


Figure 3.3 Schematic of the micro-FID stack including the quartz-Macor-quartz sandwich structure (left) and an actual picture of the micro-FID stack including the high temperature silicone sealing gaskets (right) [49].

As shown in Fig. 3.3, the top quartz plate contains the exhaust hole while the bottom quartz plate has inlet holes to supply hydrogen, air, and the sample gas. The Macor channel was sandwiched between two quartz plates with the Cr/Au electrodes. This sandwiched design creates an encapsulated structure to enhance the stability of the diffusion flame and has the advantage of preventing contamination that can occur from the environment. An actual picture of the micro-FID components for the folded flame channel is provided in Fig. 3.3 (right) which is illustrating the sandwiched stack of quartz-Macor-quartz.

3.3 Electrode Fabrication

In order to fabricate the electrodes on the quartz plates, the quartz plates were spin-coated with AZ1518 PR (Photo Resist). The AZ1518 PR was spun instead of AZ4620 PR which provides a thinner PR layer and is thus easier for liftoff. The quartz plates were then exposed in a flood exposure, which is a UV exposure device. Then, the PR patterns on quartz plates were developed in a mixture of AZ 400 K developer and DI water mixed with a 1:4 ratio (Developer: DI water). An O₂ de-scum cleaning process was performed after the development to remove unwanted residue. Chrome and gold was sputtered to a thickness of 100 Å and 1000 Å respectively. In order to obtain the final electrode patterns, the quartz plates were dipped into the 1165 PR stripper to liftoff the unnecessary PR in ultrasound and cleaned. (A step by step fabrication procedure is provided in Appendix B)

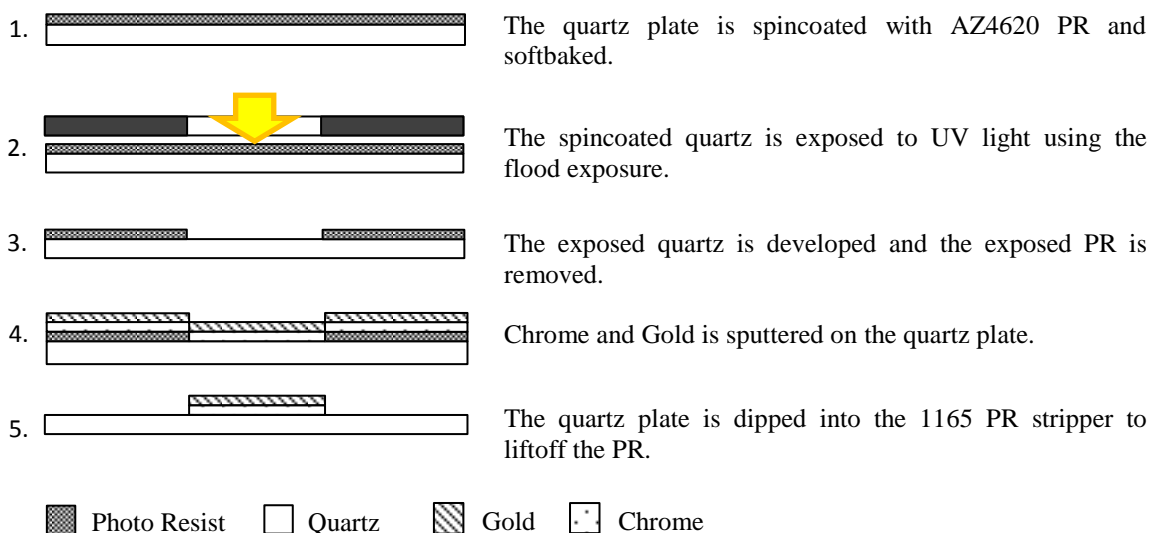


Figure 3.4 Schematic of the fabrication procedure for the Cr/Au electrodes on the quartz plate.

3.4 Experimental Setup

An aluminum package was machined and used during the initial stage of the experiments. However, as shown in Fig. 3.5, even with the rubber pads which were shielding the pogo pins from the aluminum package were still producing leakage current and causing noise signals. Thus a new package was built with Vespel and the micro-FID stack was assembled inside it as shown in Fig. 3.5. Vespel is an electrical insulation material and withstands repeated heating up to 300°C [52]. It was chosen to reduce the leakage current between the micro-FID stack and the package.

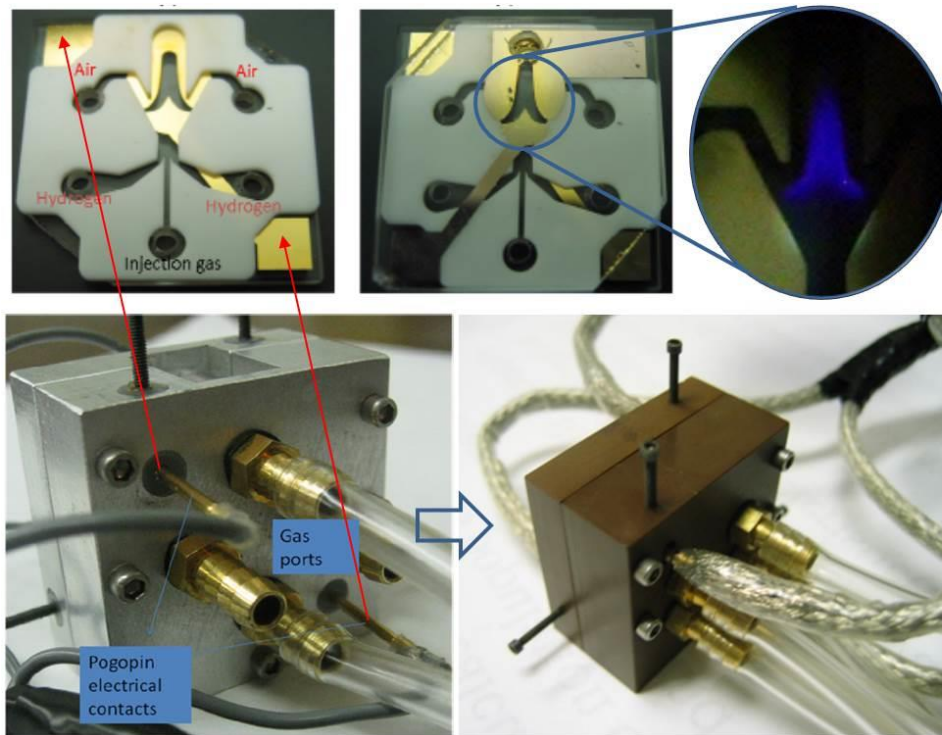


Figure 3.5 A Vespel package where the FID stack is assembled with bar fittings for tubing and supplying the gases. The Vespel package also has holes for pogo pins to serve as electrical contacts [49].

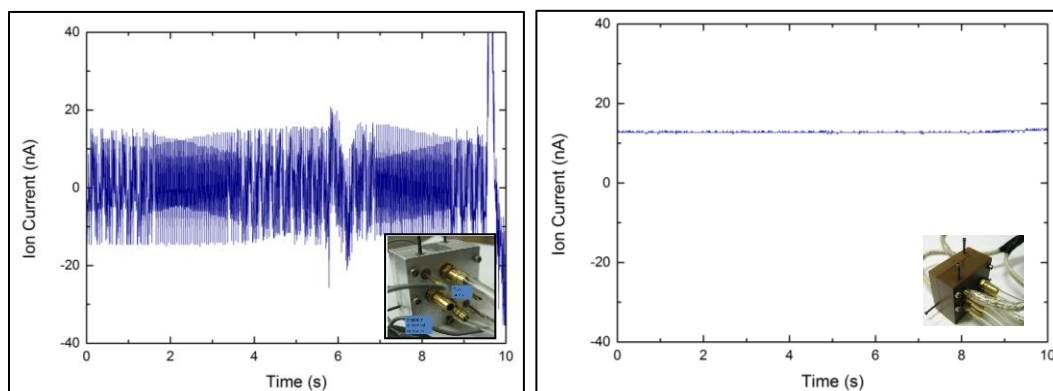


Figure 3.6 Noise comparisons between the aluminum package and the modified Vespel package. The noise was reduced by 72 times. (3.6 V \rightarrow 0.05 V)

Comparisons between the two packages are provided in Fig. 3.6 which shows the significant reduction of the noise signals by replacing the package with a better insulation material. In addition the electrical wires were shielded with metal shielding tubes and covered with a second shrink tube layer to suppress the noise signals. The initial noise band was around 3.6 V while the new package produced only 0.05 V of noise band. By replacing the material and improving the insulation the noise was reduced about 72 times.

Bar fittings were assembled to the back side of the Vespel package to connect the fluidic tube which supplies the gas. The Vespel package included injection ports for the oxidizer and hydrogen gas. Tygon tubes were used between the MFC and the aluminum package in order to supply the gas. The sample gas (Methane) was injected from the gas tank through a 6-port valve, using tygon tubes. The Vespel package had 4 holes with screws attached to fix the pogo pins which supplied the voltage and measured the ion

current. The position of the pogo pins attachment to the package aligns to the electric pad that is located at the end strips of the electrodes as illustrated in Fig. 3.3.

Figure 3.7 shows the overall experimental setup used for signal detection. Air and hydrogen were supplied and controlled with mass flow controllers from the gas tank to the micro-FID. The injection gas was metered through a 6-port valve which was actuated by a valve controller circuit. A power supply was connected to the electrodes applying 100 V. A DLPCA-200 amplifier (FEMTO Messtechnik GmbH, Paul-Lincke-Ufer 34, D-10999 Berlin Germany) was used for the evaluation for the micro-FID signal detection. After amplification, the micro-FID signal was recorded with a U3-LV data requisition board (LabJack, Lakewood, CO, U.S.).

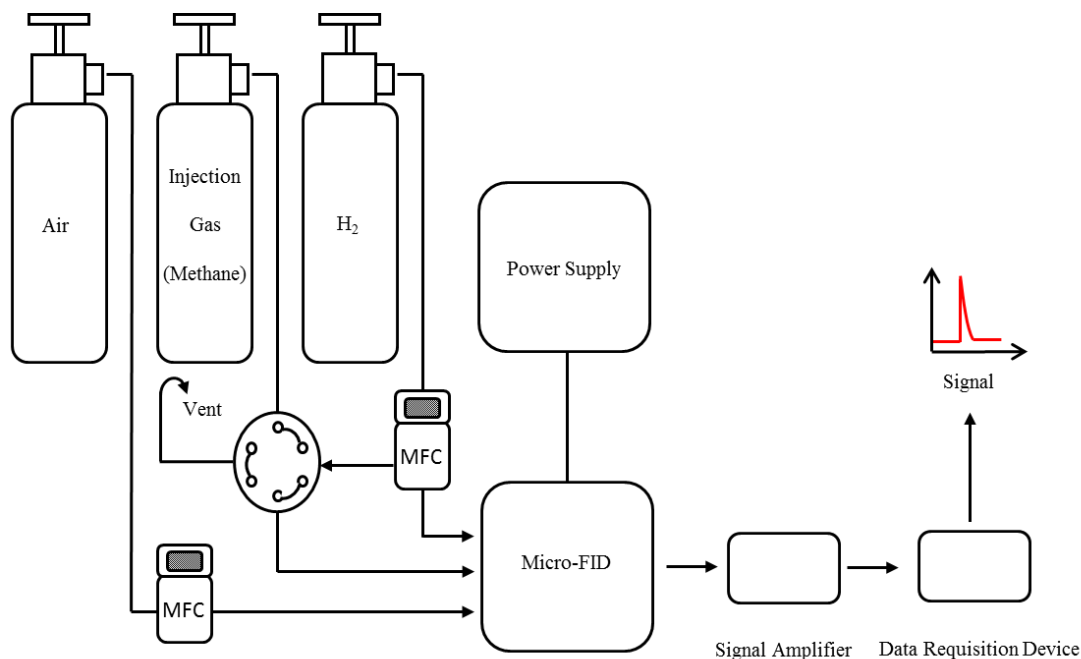


Figure 3.7 Schematic of the experimental setup, including air, hydrogen, methane gas tanks, injection system, electrical power supply, and signal detection devices.

3.5 Results and Discussion

The counter-flow channel design and the folded flame channel design were sandwiched together between two electrodes patterned on a quartz plate and tested respectively. Figure 3.7 shows a typical response of the micro-FID over time when the folded flame and counter flame channel are used respectively. A methane sample gas of 0.045 ml was injected and the flame was sustained with 120 ml/min of air and 80 ml/min of hydrogen. The picoammeter gain is set to 10^7 with 100 V applied to the electrodes.

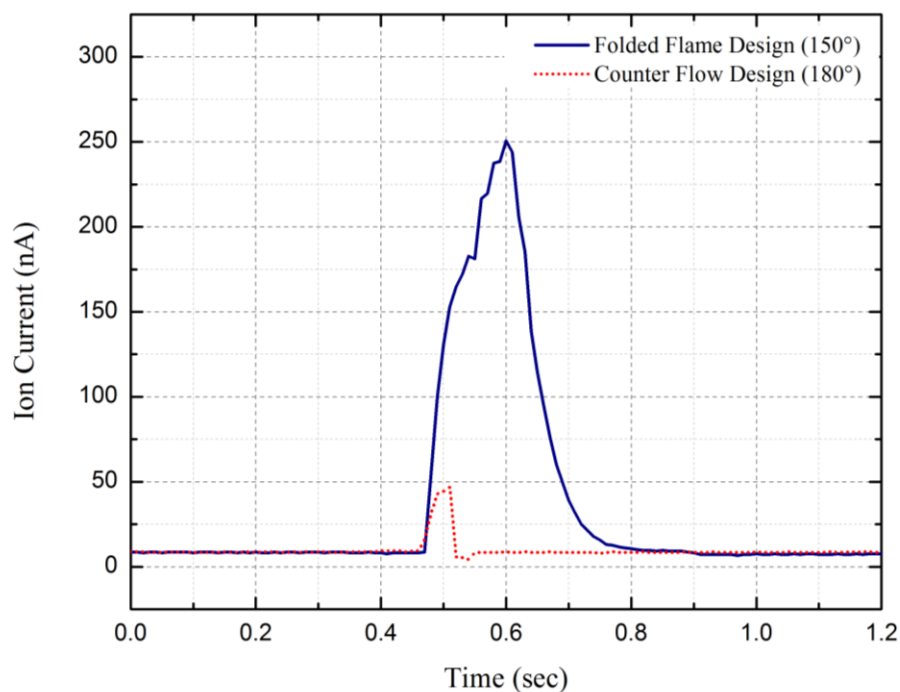


Figure 3.8 Two response signals from a folded flame (solid) and from a counter flow flame (dotted). These plots show the signal of the micro-FID over time when a sample gas of 0.045 ml of methane gas was injected. The flame was sustained with 120 ml/min of air and 80 ml/min of hydrogen. The picoammeter gain was set to 10^7 with 100 V applied to the electrodes.

The test in Fig. 3.8 was repeated 4 times and the average area of the peaks was calculated. (Table 1) The FID sensitivity S is defined as:

$$S = \frac{I_{ion}}{\dot{m}_c} \quad (2)$$

Where, I_{ion} is the ion current in A and \dot{m}_c the carbon mass flow in gC/s (gram-carbon per second). Sensitivity is thereby expressed in C/gC (coulomb per gram-carbon) [10]. Thus,

the sensitivity of the device was obtained by dividing the area of the peak with the injected amount of the sample gas. Typical results are shown in Table 3.1

	1 st run Peak Area (nC)	2nd run Peak Area (nC)	3rd run Peak Area (nC)	4th run Peak Area (nC)	Average Peak Area (nC)
Counter-flow Channel	1.6	1.0	1.0	1.2	1.2
Folded Flame Channel (150 °)	39.3	39.8	39.9	39.0	39.5

Table 3.1 Testing of Fig. 3.8 is repeated four times and each peak area is calculated and listed above. The average area of the peak is about 1.2 nC and 39.5 nC for the counter-flow flame design and folded flame design respectively. This implies that for 0.045 ml of injected methane at 3 atm (45 psi) in room temperature, the peak area was about 34 times larger for the folded flame design

The average peak area was about 1.2 nC and 39.5 nC for the counter-flow flame design and folded flame design, respectively. The sensitivity was calculated by dividing each peak area with the injected amount of gram-carbons of 0.045 ml of methane. Results are shown in Table 3.2.

	Counter Flow (180 °)	Folded Flame Design (150 °)	Conventional macro- FID [11]
Sensitivity (mC/gC)	0.04	1	15

Table 3.2 Micro-FID sensitivity as calculated by dividing each peak area with the injected amount of gram-carbons of 0.045 ml of methane.

The sensitivity obtained with the counter-flow design was 0.04 mC/gC. The sensitivity attained with the folded flame design provided a higher sensitivity of 1 mC/gC which was about 25 times higher compared to the counter-flow design. This is a spectacular increase in sensitivity, which shows that the folded flame design provides higher ionization efficiency and enhances ionization with less leakage of the analytes compared to the counter-flow flame. The effect of detailed micro-combustion physics on signal quality is therefore evident. However, as Table 3.2 clearly indicates the highest sensitivity achieved with the folded flame configuration was still about 15 times less than the conventional FID sensitivity introduced [11]. The sensitivity can be improved even more by injecting the analytes through a narrower port which will decrease the time duration of the signal, thus increasing its peak value and resulting in higher sensitivity.

Chapter 4: Signal Strength Enhancement

4.1 The need for enhanced signals

The results of the previous sections established that the folded flame channel design was the desired channel configuration for the micro-FID. However, the sensitivity level of the developed micro-FID was still relatively low compared to the commercial macro-FIDs. Also the overall flow rate needed to be reduced in order to achieve portable applications. The goal is to achieve portability of the device. Thus the device needs to be able to operate with fuel rates that can be supplied with portable sources. Since a commercially available portable electrolyzer [55] can produce an oxygen flow rate of 32 ml/min and hydrogen flow of 64 ml/min. Thus the goal is to develop a micro-FID that can operate within this range of flow rates.

The goal was to reduce the overall fuel consumption while still obtaining low MDL which is defined as the minimum concentration of a solute passing through the detector that can be unambiguously distinguished from the noise. Generally this means a measurement with a signal-to-noise ratio equal to at least two. Several tactics were used to this end, including modification in channel geometry, as well as introduction of an oxygen stream mixed into the air flow in order to enhance ionization. Also, a portable electrolyzer was used in order to supply oxygen and hydrogen gas. The motivation of this line of work was to achieve a low minimum detection limit through the enhancement of signal strength as opposed to reduction of the noise level, which will be independently discussed in a following chapter.

4.2 Flame Observation

The previous micro-FIDs which were introduced in Chap. 4 had a fuel consumption rate which was too high to achieve the target of a portable device that would be fueled through electrolysis of small amounts of water with a portable battery. A commercially available portable electrolyzer can produce hydrogen from distilled water with a production rate of 65 ml/min [55]. The electrolyzer was connected to a parallel 6 single cell Lithium battery with maximum output of 3.7 V and 4 A. This battery was able to produce a hydrogen flow rate of 25 ml/min for 8 hours applying 1.8 A to 2.0 A to the electrolyzer. Here, the heat dissipation for the flame with a hydrogen flow rate of 25 ml/min was calculated using the mass flow rate and the lower heating value (LHW) of hydrogen which was around 4×10^{-8} kg/s and 120, 000 kJ/kg respectively. The heat dissipation of the flame was approximately 4 W which could be taken care of by natural convection without the need to resort to expensive insulations.

In order to achieve a working device within this flow rate, smaller silicon channels were fabricated with the same 150° angle configuration between the air and hydrogen stream. Channel sizes were reduced about 60% in cross-sectional area in order to reduce fuel consumption rate as indicated with arrows in Fig. 4.1.

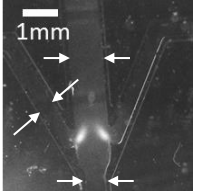

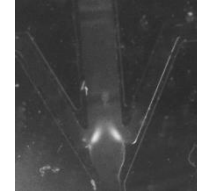
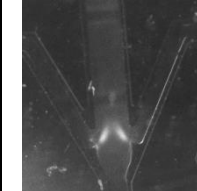

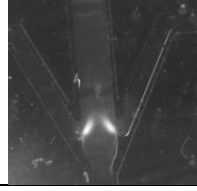
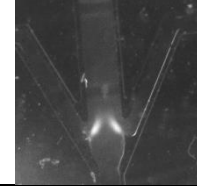
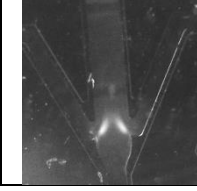
	Air (35 ml/min)	Air (44 ml/min)	Air (53 ml/min)	Air (62 ml/min)
H ₂ (25 ml/min) O ₂ (12.5 ml/min)				
H ₂ (26 ml/min) O ₂ (13 ml/min)				

Table 4.1 Flame structures obtained with the channel configuration of Fig. 2.3-(c). Channel (shown with arrows in the top-left panel) sizes were reduced about 60% in width, in order to reduce the fuel supported by hydrogen and oxygen supplied by a portable electrolyzer.

The results of Fig. 4.1 present non-premixed hydrogen-air flames that operated with hydrogen flow rates provided by a portable electrolyzer. The flame was sustained with reduced hydrogen flow rate which was about 3 times less than the flow rate that was used before the channel size reduction. This specific flow rate was not significantly lower than the flow rate used in large scale FIDs which is suggested to be around 40 ml/min. However, the hydrogen flow rate that was used for our device required significantly lower flow rate of oxidizer compared to the large scale FID and used only 35 ml/min instead of 450 ml/min. The flames were encapsulated safely in a light portable silicon structure and their folded structure generated relatively small strain on the flame, thus providing large residence times that minimized analyte loss. Such an encapsulated micro-flame can be the heart of an agile and portable micro-FID.

4.3 Design and Modification

The size of the Macor channels in the micro-FID was reduced as shown in Fig. 4.2. The width of the channels was reduced by a factor of two. The thickness of the channel was kept as 750 μm , and as shown in Fig. 4.2 the oxidizer channel width was reduced from 1 mm to 500 μm . Also, the hydrogen channel and the injection channel were reduced from 500 μm to 250 μm . The round injection port size for air, hydrogen, and injection flow remained the same. Air was replaced with oxygen in order to provide higher ionization efficiency with less flow, and simulate the envisioned portable devices that will operate on oxygen provided from an electrolyzer. Oxygen and hydrogen were metered through the ports shown in Fig. 4.2. The port in the bottom was used for the injection gas. Pentane gas was injected by connecting the micro-FID to a GC (Agilent GC 7890A). In our experimental work, we utilized several hydrocarbons in order to make sure that the reported results were not analyte-specific.

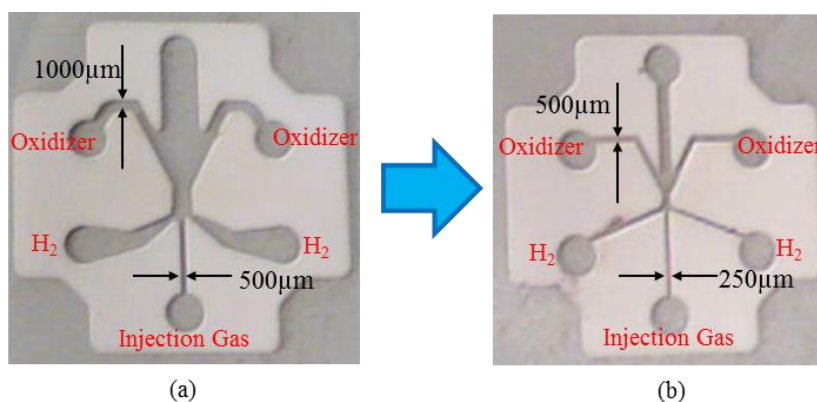


Figure 4.2 (a) Previous larger Macor channel (b) Modified smaller Macor channel.

Dead volumes in the microfluidic circuit cause broadening of the FID response in time, because the injected fluid has a longer residence time in the apparatus. For a given number of carbon atoms, the time-integrated signal will remain the same, so the peak value of a broadened signal will be lower, and therefore more difficult to distinguish. This can limit the MDL of the instrument. In order to confine the injection gas stream and prevent broadening during injection, a modified injection port was introduced as shown in Fig. 4.3.

The injection port size was reduced in order to minimize dead volumes. The large injection port that was introduced in the previous designs had a larger dead volume between the column and the channel. The red striped region in the schematic represents the dead volume inside the injection port. Once the injection gas reaches the end of the column it will fill this region and resulting in lower maximum signal. In order to reduce the dead volume, the injection port was reduced to a simple straight channel. As indicated in Fig. 4.3, the cross section view shows the reduced dead volume indicated in a red striped region. The injection port width was especially designed to match the column outer diameter that was connected to the GC. This modification however, does not mean that more ions were collected. The importance of the particular modification was that the signal got sharper by confining the injection stream and minimizing the dead volume. These sharper signals can improve the sensitivity since sharper peaks are easier to detect and distinguish from noise signals.

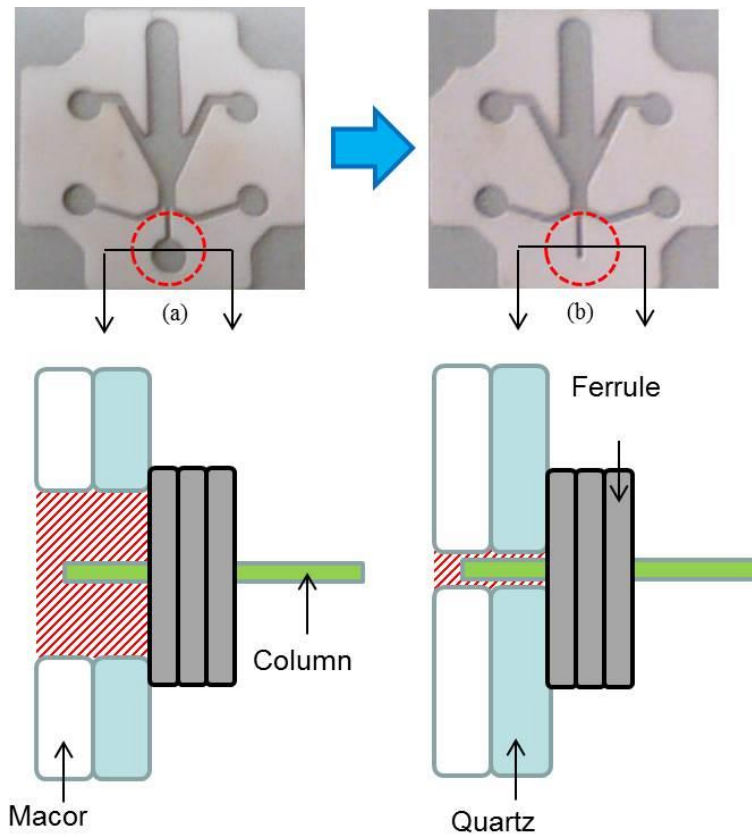


Figure 4.3 (a) Previous Macor channel with larger injection port (b) Modified Macor channel with smaller injection port.

Flame position and shape are important in order to achieve a steady and strong signal, as discussed in Chap. 2. Therefore it is important to sustain a stable flame at the desired place and shape. As discussed in the previous section, in order to reduce the overall fuel consumption rate, the channel width was reduced. However during this process it was observed that the flame was anchoring at the exhaust area. As shown in Fig. 4.4 initial designs included sharp corners at the exhaust area and the flame anchored at this region. These sharp corners indicated in Fig. 4.4 worked as anchor points, and needed to be smoothed out.

This led to the idea to employ the anchor points in our channel design in order to increase the stability of the flame. As shown in the schematic, in Fig. 4.4 the anchor points guides the flow around the anchor tips and provides the flow a longer residence time. This effect leads to anchor the flame at the anchor point due to the relatively higher residence time of the flow and higher local temperature.

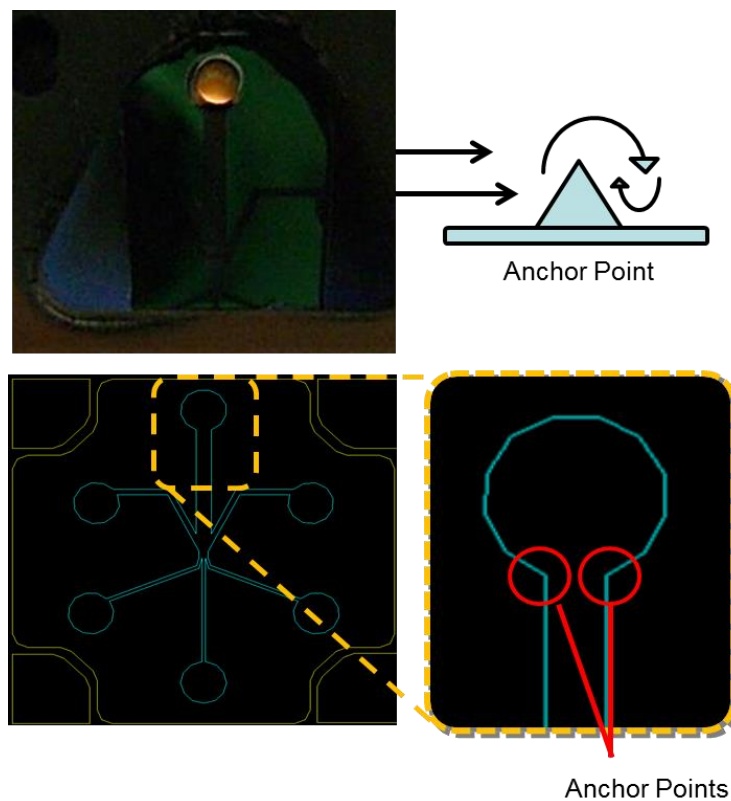


Figure 4.4 Anchoring effect on the flame at the exhaust area due to sharp corners in the hardware.

Anchor points were designed and introduced into the burner cavity of the silicon channel. These anchor points were located inside the burner cavity, in the middle region of the channel where the flame sat, as shown in Fig. 4.5-(b). Anchor point positions were designed based on the flame pictures that were taken during the flame observation process.

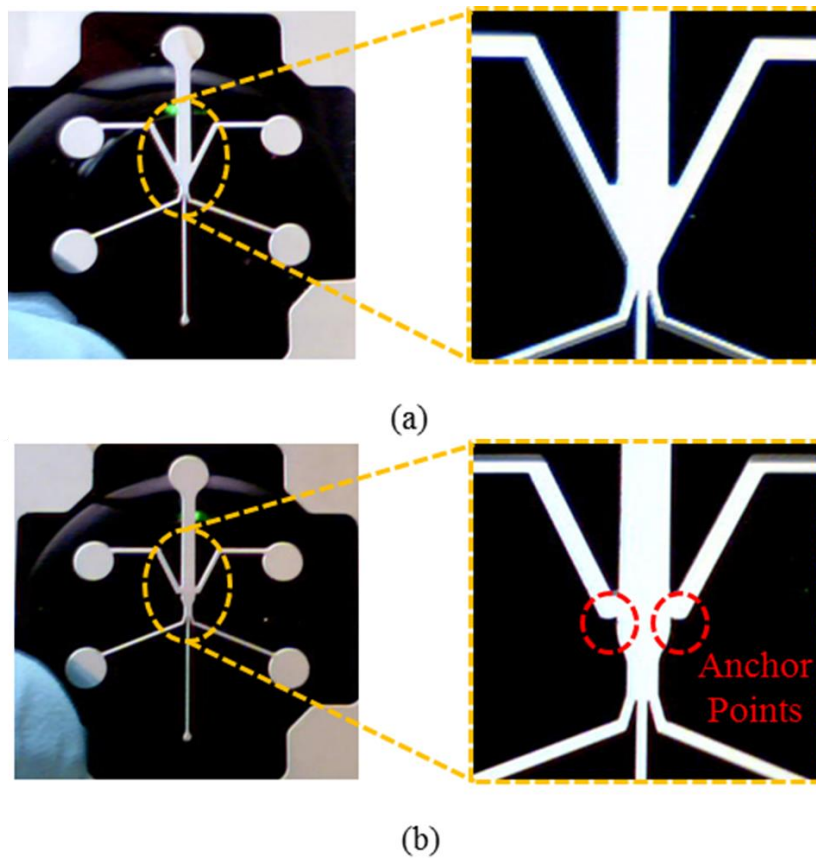


Figure 4.5 (a) Smaller Macor channel (b) Modified smaller Macor channel with anchor points.

4.4 Experimental Setup

The same Vespel package that was introduced in the section 3.2 was used. A Gas chromatograph (GC) (Agilent GC 7890A) was used to have better control over the injection properties such as the pressure, flow rate, temperature of the injection gas including the carrier gas as well as the sample gas itself. An electrolyzer was used to supply the hydrogen gas and oxygen. A portable electrolyzer is an absolute pre-requisite for the portability of the micro-FID. The flow of hydrogen and oxygen gas was controlled by adjusting the current that was supplied from a power supply to the electrolyzer. Additional oxidizer was metered from a gas tank with a mass flow controller. In order to ignite the flame additional air was required at a flow rate of approximately 30 standard ml/min, which can be easily provided by a small fan in a practical application. The picoammeter was set to an amplification of 10^7 and the power supply applied 100 V across the electrodes. A schematic of the apparatus is provided in Fig.4.6.

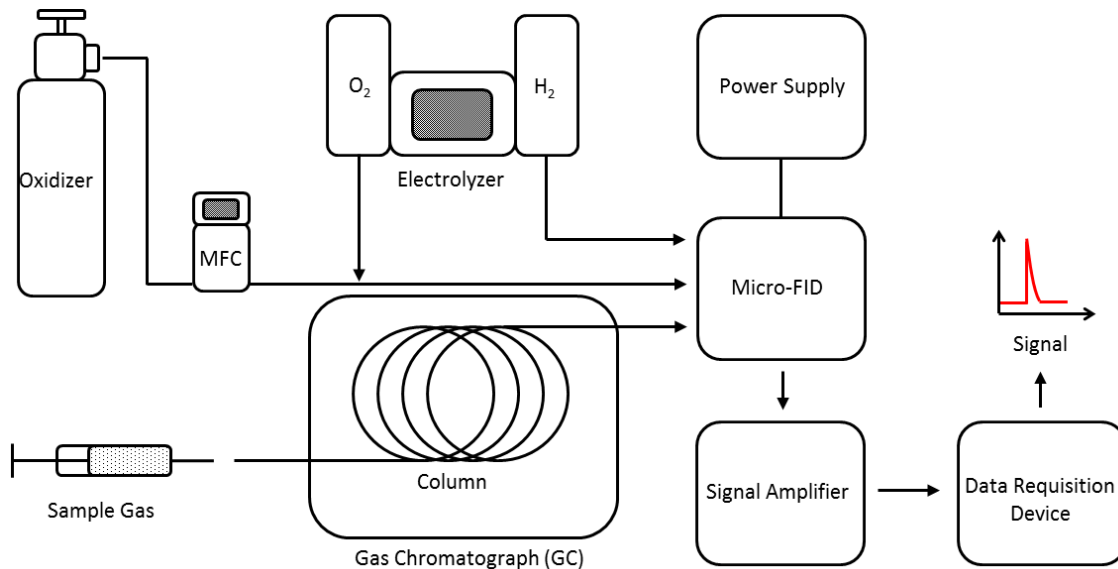


Figure 4.6 A schematic of the overall experimental setup

4.5 Results and Discussion

The micro-FID with channels of reduced diameter was tested with a flow rate of 34 ml/min (17 ml/min from the electrolyzer and 17 ml/min from the gas tank) of oxygen and 34 ml/min of hydrogen. This corresponded to a speed of the oxygen stream equal to 1.5 m/s and hydrogen stream of 2.0 m/s. The Reynolds numbers were 191 and 3 for the air stream and hydrogen stream respectively and the strain imposed on the flame was 720 s^{-1} . The extra oxygen flow which was produced from the electrolyzer allowed us to reduce the overall fuel consumption. Mixing an oxygen stream into the air stream increased the overall flame temperature and sustained a flame with less fuel.

Experiments were performed by reducing the injection amount of pentane in order to achieve the MDL. The result in Fig. 4.7 shows the detected signal for each injection of

pentane. Due to the isomers multiple signal peaks were detected. In order to inject small amounts of pentane the GC was operated in a split mode. Starting with the highest injection amount of 0.01 μl (3 μg) of pentane produced the highest peak and peak area. Reducing the injection amount of pentane resulted in the reduction of the signal. The smallest injection amount detected was 0.001 μl (300 ng) of pentane. The area of each injection peak was calculated. The sensitivity was calculated similarly to the process of section 4.5 and the results are shown in Table 4.1. A sensitivity of 1.34 mC/gC was obtained with the larger folded flame channel while the smaller channel had an average sensitivity of around 5.51 mC/gC. Comparing the results from Table 3.1 and Table 3.2, we can see that the smaller Macor channel and the introduction of oxygen increased the sensitivity about 3.7 times.

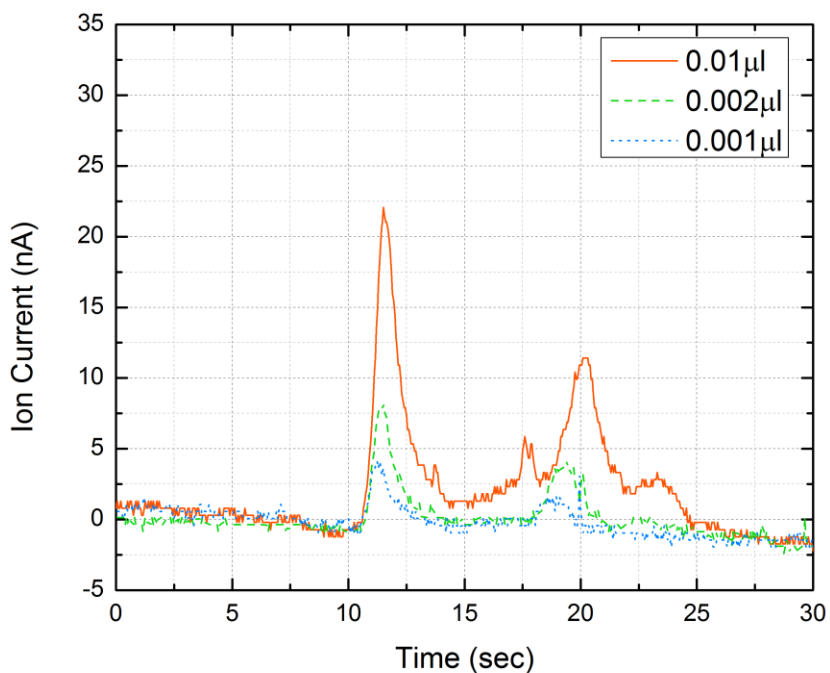


Figure 4.7 Result of ion current measurements during pentane injection.

Pentane Injection (ng)	Peak Area (nC)	Sensitivity (mC/gC)
3000	64.6	4.1
600	17.3	5.5
300	8.6	5.5

Table 4.2 Signal strength during pentane injection. The table reports the peak area for each injection and the calculated sensitivity of the micro-FID using the narrower Macor channel.

The effect of a reduced size injection port is shown in Fig. 4.8. The sensitivity was maximized when the flow rate was set to 60 ml/min of oxygen, 35 ml/min of hydrogen. This corresponded to a speed of the oxygen stream equal to 2.7 m/sec and hydrogen stream of 2.1 m/sec. The Reynolds numbers were 337 and 3 for the air stream and hydrogen stream respectively and the strain imposed on the flame was 720 s^{-1} . Hexane was injected using the GC with a helium carrier flow of 2 ml/min. The injection volume was $0.1 \text{ }\mu\text{l}$ with a split ratio of 20 to 1, which reduced the actual injection to 1/20 of the total injection amount ($0.005 \text{ }\mu\text{l}$). As illustrated in Fig. 4.8, the channel with the narrow injection port provided a maximum signal that was approximately 30% increased in height and a total signal (i.e. integrated surface area) of that was 27% larger than the one with the larger injection sport. The maximum ion current increased from around 32 nA to 43 nA and produced a sharper peak. It was thus determined that if the dead volume was reduced and the injection stream became more confined, the micro-FID signal was substantially sharper. A sharper signal (i.e. a larger maximum) is preferred if the integrated area is the same, because the signal can be distinguished more easily against background noise.

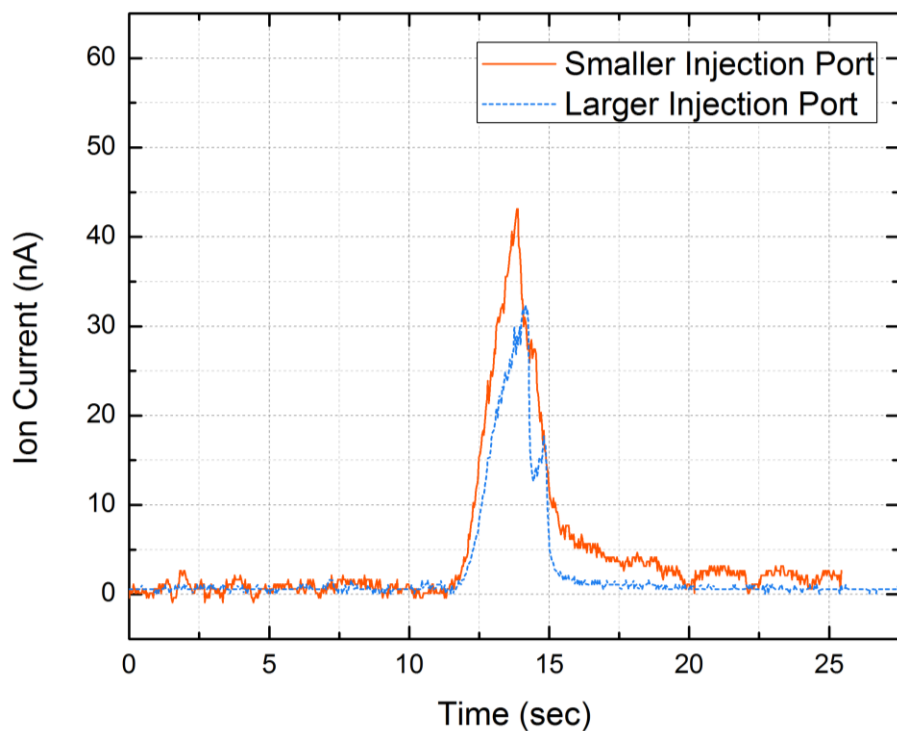


Figure 4.8 Comparison between the reduced size injection port and the large injection port.

Figure 4.9 shows a comparison of a silicon channel with and without the anchor points of Fig. 4.5. The experiment was performed with a flow rate of 11 ml/min of oxygen, 21 ml/min of hydrogen, and 35.5 ml/min of air. Hexane was injected using the GC with a carrier flow of 2 ml/min and an injection volume of 0.1 μl with a split ratio of 20 to 1. As shown in Fig. 4.9, the channel with the anchor point structure provided a stronger ion current peak signal. It can be thus determined that the anchor point provided a stable flame that increased ionization efficiency.

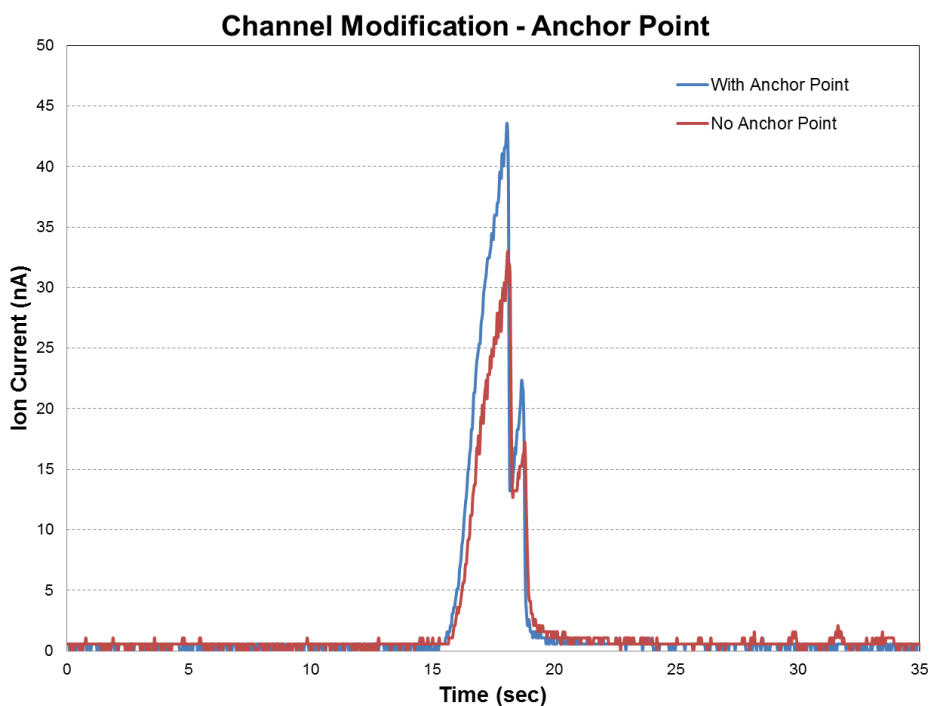


Figure 4.9 Comparison between the channel designs with and without the anchor points. A flow rate of 11 ml/min of oxygen, 21 ml/min of hydrogen, and 35.5 ml/min of air was supplied. Hexane was injected using the GC with a carrier flow of 2 ml/min and an injection volume of 0.1 μ l with a split ratio of 20 to 1.

Chapter 5: Noise Reduction

5.1 Fundamental considerations

The MDL can be increased by improving the signal or reducing the noise [53]. The work to improve MDL by increasing the signal strength was introduced in chapter 4, while here we will focus on the noise reduction. The noise is usually defined as the peak-to-peak noise which is the difference between the minimum and the maximum value of the base line signal [4]. Since the FID is mass sensitive, and thus sensitive to the injection amount, as the sample mass reduces it gets harder to distinguish from the noise signal. Thus, when detecting small amount of samples the noise plays a critical role, reducing the noise important to achieve a high sensitive micro-FID.

As explained in Chapter 1.2.1, the material of the burner is very important in order to sustain a steady micro-flame inside the channels. Flame unsteadiness or instability can generate noise in the FID response. Another source of noise is graduate fouling and degradation of the channel material and the electrodes. In particular, after running the experiment for about 50 times it was observed that the channel wall near the flame melted.

As shown in Fig. 5.1, one of the channel tips was melted away. In order to verify the effect of the melted channel structure, a quartz plate was sputtered with gold and was assembled inside the micro-FID for testing. The flame inside the channel melted the gold surface and left a mark similar to the flame profile as shown in Fig. 5.1. A zoomed view shows clearly the flame profile with the melted tip of the Macor channel indicated with

an orange circle. The folded flame was not symmetric but shifted to one side. This could be critical since the electrodes were initially designed for a specific folded flame structure. Flame shapes that do not follow the design of the electrodes can cause noise signals as discussed in chap.3. Therefore new materials were needed to avoid channel melting and flame shifting.

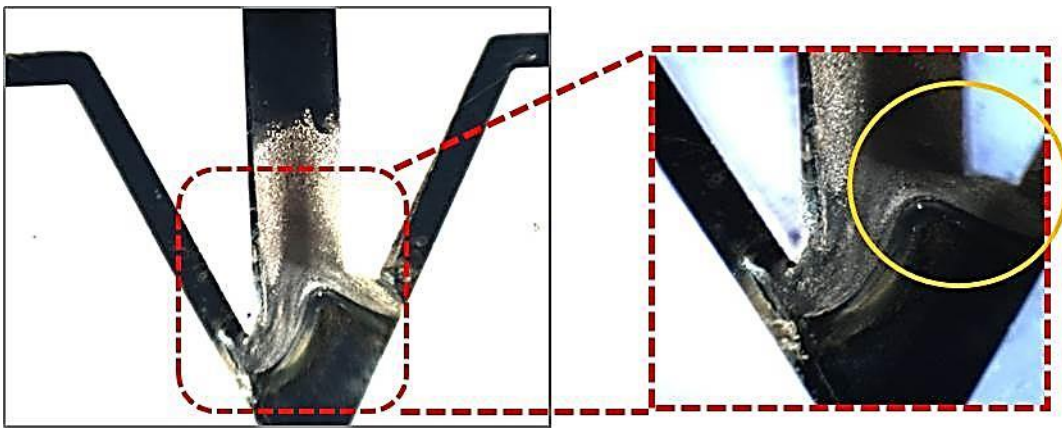


Figure 5.1 Macor channel melting due to the high flame temperature. The melted region of the gold pads represents the flame profile which is shifted to one side.

Macor channels were replaced with silicon oxide channels which had a higher melting temperature of 1700°C and had very low electrical conductivity, similar to Macor ($10^{16} \Omega\text{-cm}$). The silicon channels were fabricated with silicon on insulator (SOI) wafers which contained an insulation layer inside the silicon wafer as shown in Fig.5.2. This additional insulation layer improves electrical insulation and prevents electrical shorts. Silicon oxide layers were grown on the surface when fabricating channels with regular

silicon wafer. However, small scratches on the surface were critical leading to electrical shorts. For this reason, silicon channels were not used during the initial stage of this research and Macor channels were machined instead. Replacing the channel material to SOI wafers allowed us to reduce the electrical short as well as the melting problem.

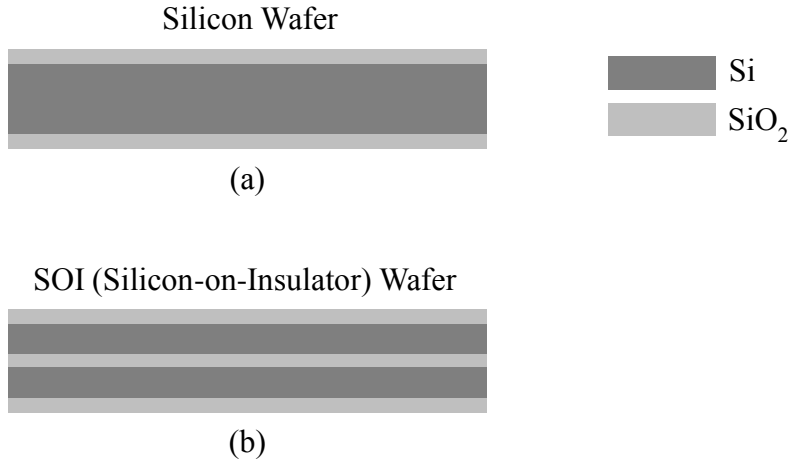


Figure 5.2 (a) Cross view of a silicon wafer with silicon oxide grown layer on the outside. (b) Cross view of a SOI wafer with silicon oxide grown. The SOI wafer provides better electrical insulation due to the additional silicon oxide insulation layer inside.

Additional improvements were applied to the channel design. During the experiments it was observed that the electrical shorts were frequently caused by the lack of insulation on the side walls of the channels. Thus, channels were fabricated with an additional step as shown in Fig. 5.3. Regular silicon wafers and SOI wafers exhibited electrical short problems caused around the side walls of the channels. Therefore, an additional step layer was built in as shown below in Fig. 5.3. This modification improved the insulation at the side walls. Using the fact that an insulation layer was embedded

inside the wafer, one side of the channel was fabricated with a slightly smaller size, which created an additional barrier preventing electrical short along the side walls.

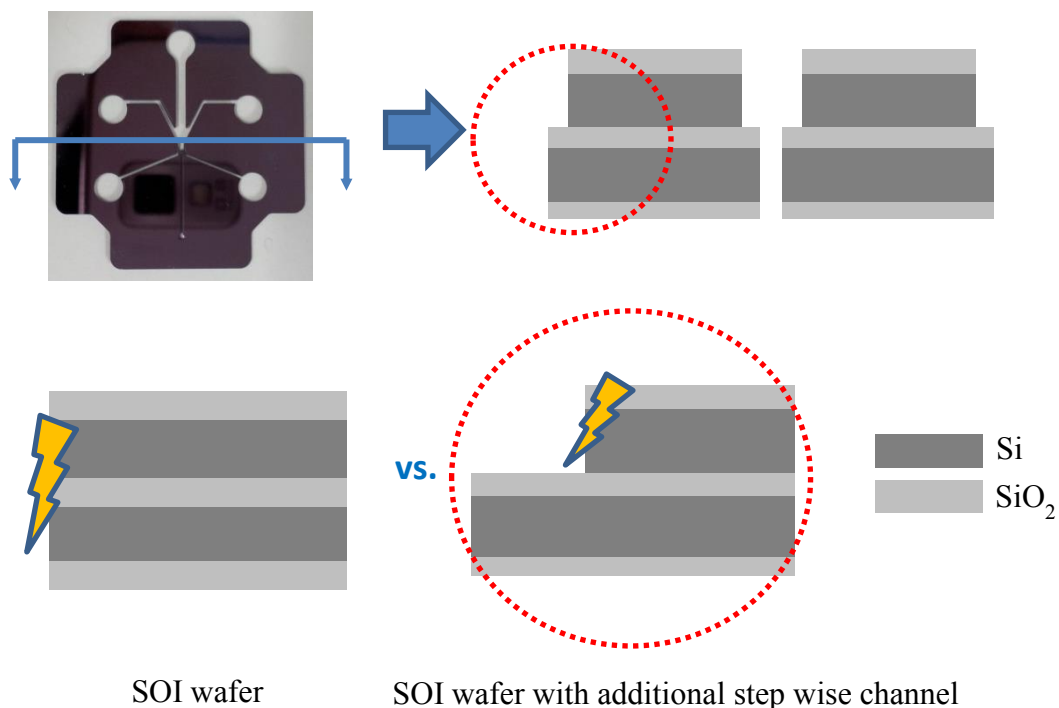


Figure 5.3 Side view of the SOI channel. An additional step was created inside the channel. Fabricating an additional step to the channels with smaller widths improved the electrical insulation along the side-walls.

Additionally, in order to reduce noise signals, a Faraday cage was built to shield the micro-FID from electric noise. An actual picture is shown in Fig. 5.4 which shows the assembled Faraday cage, the pogopins for the voltage supply to the electrodes package. The cage included two BNC cable ports for the electrical connections. The

entire package was grounded to a single ground with all the other electrical components, such as the amplifier the circuit board.

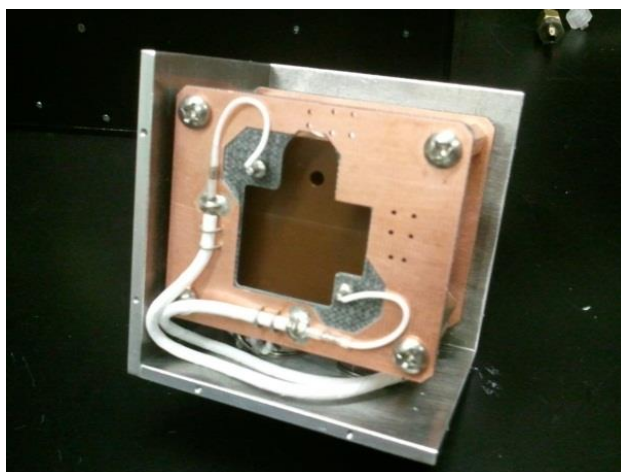


Figure 5.4 Picture of the Faraday cage and micro-FID built inside the prototype of a portable GC from Cbana Labs. The Faraday cage built to shield the entire Vespel package and the micro-FID inside. The Faraday cage included BNC connectors for electrical connections. The entire package was electrically grounded to a single ground with the amplifier and the circuit board. (Courtesy of Cbana Labs)

5.2 Fabrication

The fabrication procedure for the reduced-noise apparatus was very similar to the fabrication steps introduced in section 2.3. Several steps were added in the fabrication recipe. The same fabrication procedure was used for the SOI wafer till the developing step. An additional step was needed during the silicon etching step. Instead of a through etch, the wafer was etched till it reaches the silicon oxide layer that was embedded in the

middle of the wafer. Now the wafer was dipped into the HF etchant to remove the silicon oxide layer. This additional step was needed since the ICP-DRIE is not ideal to etch the silicon oxide layer. Once the silicon oxide layer was removed, the wafer was etched with the ICP-DRIE till it etched through. Similarly to the fabrication steps of section 2.3, the PR was removed using the 400T PR stripper. Before growing an oxide layer for the electrical insulation layer the silicon channels were cleaned using a SC-1 cleaning process. After the cleaning procedure, the silicon channels were loaded into the thermal oxidation tube furnace to grow 5000 Å of oxide on the silicon channels.

5.3 Results and Discussion

In order to reduce noise, a Faraday cage was built to shield the micro-FID. Shielding and grounding of the micro-FID package with the picoammeter was extremely important, since the noise was also amplified during the signal collection. Figure 5.5 shows two background signals using the SOI channel with and without the Faraday cage. The experiment was performed with 11.5 ml/min of oxygen, 23.0 ml/min of hydrogen, and 36.0 ml/min of air. The noise with the Faraday cage has been reduced more than 43 times compared to the noise without the Faraday cage.

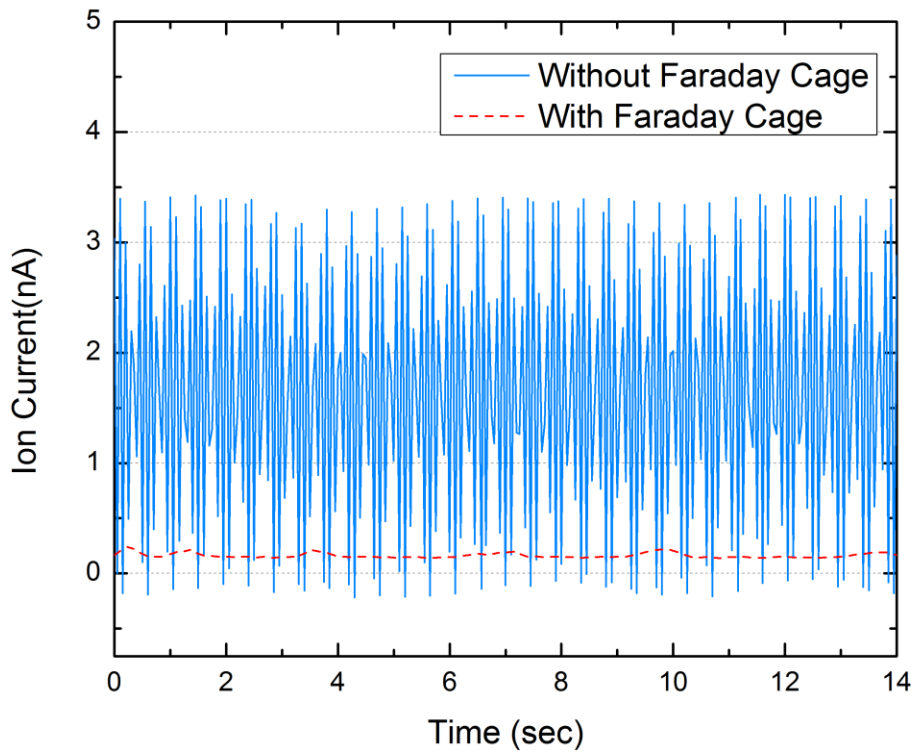


Figure 5.5 Two background signals with and without the Faraday cage both using the SOI channel [49, 56].

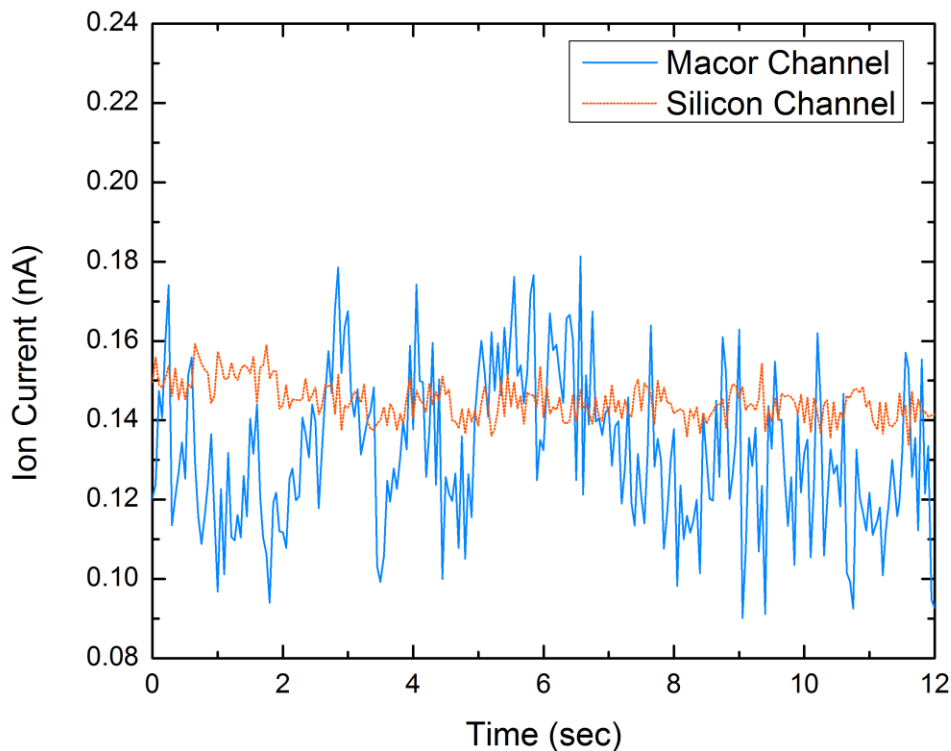


Figure 5.6 Noise reductions when a SOI channel was used versus the Macor channel. Both noises were tested with the Faraday cage [49, 56].

The use of the SOI channel reduced the noise level. The result shown in Fig. 5.6 was obtained with the same flow conditions used in the previous experiment. When testing the noise of both the silicon channel and the Macor channel the Faraday cage was used. From the results of Fig. 5.6 it can be determined that the noise level produced when using the silicon channel combined with the Faraday Cage was less than 200 μV , which corresponded to 20 pA. This was almost 4 times smaller than the noise of the micro-FID with the Macor channels. Hexane was injected from a GC to the micro-FID. A current of 1.8 A was applied to the electrolyzer to produce a flow rate of 11.19 ml/min

for oxygen, 22.39 ml/min for hydrogen, and 23.8 ml/min for the air. The minimum detection limit was reached when 0.00002 μl of hexane was injected. The average sensitivity of the device was 0.056 C/gC which was slightly improved after using silicon channels and the insulation of the Faraday cage.

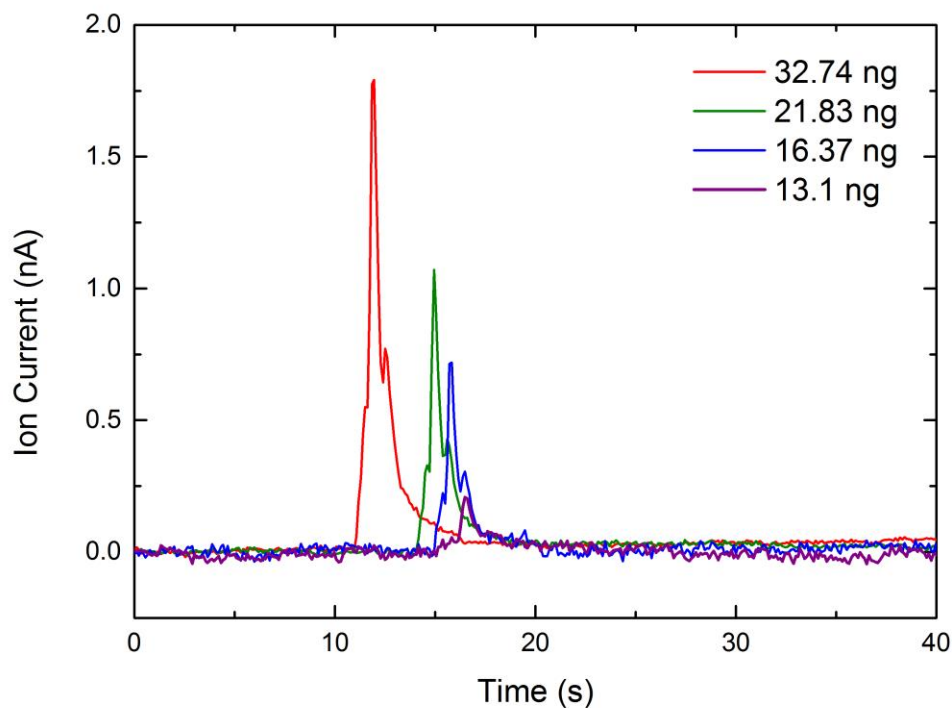


Figure 5.7 Determination of the minimum detection level for hexane injection.

Results in Fig. 5.7 shows the responding ion current signals obtained for each corresponding hexane injection amount. In Fig. 5.7 the ion current signals are shifted for each different injection. However this time difference was caused due to simple manual operation of recording the data and not due to other critical reasons. Reduced noise

resulted in an increase of the signal-to-noise ratio and a decrease of the minimum detection level. Integrated areas corresponding to different injected quantities of hexane were calculated. The sensitivity of the modified device was calculated using the integrated area and the injection amount. The results of this process are shown in Fig. 5.3 and Table 5.1.

Hexane Injection (nl)	Measured Charge (nC)	Total Injection Mass (ng)	Injected mass of carbon (ngC)	Sensitivity (mC/gC)
0.1	2.6	65.5	393	5.5
0.05	1.3	32.7	196	6.5
0.033	8.0	21.8	131	6.1
0.02	3.5	13.1	79	4.4

Table 5.1 Sensitivity measurements in the micro-FID especially designed for reduced noise.

This improved performance allowed us to detect a mixture of gases using the GC. The goal was to separate and detect the NASA Spacecraft Maximum Allowable Concentrations (SMAC) list of compounds [54] in the cabin air that is desired for ensuring crews' health. Fig. 5.8 shows the separation and detection of 17 compounds from the SMAC list including benzene, toluene, ethylbenzene, xylenes (BTEX), Methanol, Isoprene, Methylenechloride, Nitromethane, Methyl ethyl ketone, Chloroform, 1,2-dichloroethane, 1-butanol, Trichloroethane, 2-ethoxyethanol, 4-methyl-2-pentanone, Hexanal, and Diacetone alcohol. The test conditions were the same as in Fig. 5.7 with the total injection volume of 0.01 μ l and a split ratio of 100:1. The separation was carried out at room temperature and the same coated. The inset plot in Fig. 5.8 shows zoomed-in

peaks from 0 to 50 seconds that are very closely spaced. All the 17 compounds were clearly separated in less than 200 seconds.

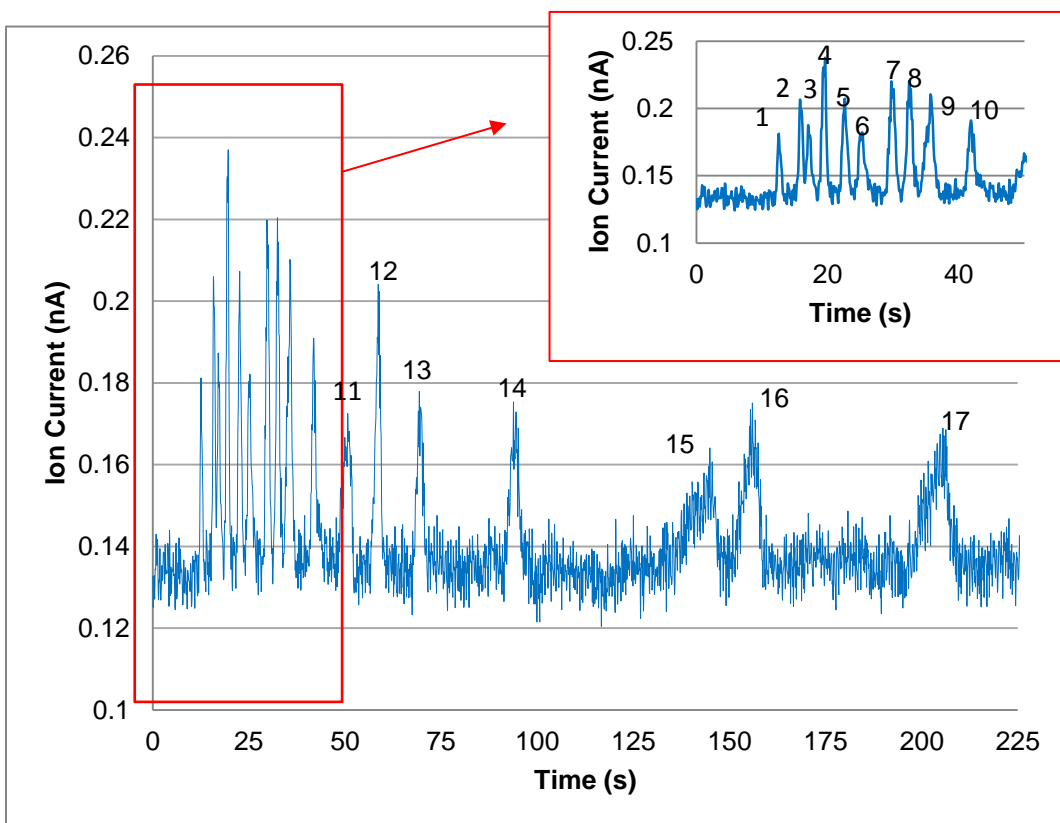


Figure 5.8 Spectrum of the 17 SMAC compounds. All the 17 compounds including BTEX are clearly separated and detected [56].

Chapter 6: Determination of optimal operational conditions

In this chapter, the work is focused on the influence of operating parameters on the sensitivity of the micro-FID that was introduced in the previous chapters. The influence of hydrogen flow, oxygen flow and air flow, saturation voltage on the device performance is examined. In addition, the minimum detection limit (MDL) of the device is analyzed by observing the signal output and noise of the device. Special emphasis is placed on the determination of the flow conditions that maximize the signal-to-noise ratio of the micro-FID.

6.1 Optimization of the oxygen/hydrogen mass flow ratio

Device performance can be improved by increasing its sensitivity and achieving a low MDL. This can be achieved by controlling the gas flow rate and examining the resulting signals. In order to examine the overall performance of the micro-FID with respect to the gas flow rate, the signal to noise ratio was calculated and the overall collected ion current responding to the sample injection was taken as a reference value.

The experiment was performed using the channel design introduced in Chap. 5. In order to control the gas flow rate, the electrolyzer was connected to a power supply and the applied current was varied. It has been suggested in previous studies that increasing the air flow can result in stronger signals due to an increase in chemi-ionization of the CH radicals, as suggested in [11]. Thus, an air tank was connected through a mass flow controller in order to record signal response respect to a function of air flow.

An amount of 0.01 μl of benzene gas was injected into the micro-FID using the injection pump of a GC. Helium gas was used as carrier gas with a flow rate of 0.4 ml/min. The air flow rate was changed from 22 ml/min to 45 ml/min. Once the air flow rate exceeded 45 ml/min the flame became unstable and produced noise signals and even extinguished with higher flow rates. The hydrogen flow rate was changed from 25.9 ml/min to 34.5 ml/min. The injection of benzene gas was repeated three times for each condition.

In Fig. 6.1 average signals are presented from the three repeated injections for each set of flow conditions. Similarly to the observations of [11] an increase in the flow rate yielded stronger signals. Results in Fig. 6.1 also showed that not only the increase in air flow, but also increasing the hydrogen and oxygen flow rate from the electrolyzer yielded in stronger signals. (Oxygen was always supplied half of the amount of the hydrogen flow from the electrolyzer.) From the results of Fig. 6.1, it is evident that the higher the air flow rate, the stronger the effect of hydrogen flow and oxygen flow rates on signal strength.

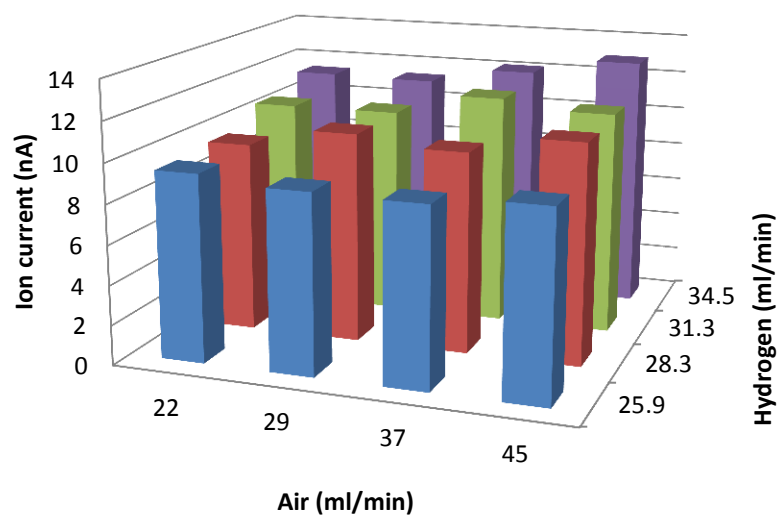


Figure 6.1 The plot shows the response signal of the ion current signal. Air was varied from 22 ml/min to 45 ml/min and hydrogen flow was varied from 25.9 ml/min to 34.5 ml/min and an oxygen flow half of the hydrogen flow was supplied. Each data represents the average signal height of three repeated benzene gas injections of 0.01 μ l.

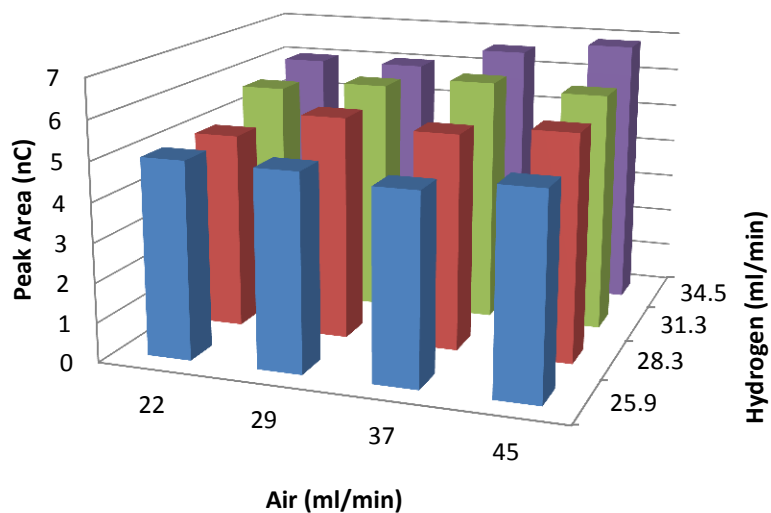


Figure 6.2 The plot shows the peak area which represents the collected ion current of the micro-FID. Air was varied from 22 ml/min to 45 ml/min and hydrogen flow was varied from 25.9 ml/min to 34.5 ml/min and an oxygen flow half of the hydrogen flow was supplied.

Peak area of each signals were calculated and plotted in Fig. 6.2. This result was also obtained by taking the average of the area of the three repeated injections. The peak area of the signal represents the collection rate of the produced ions. More ions were collected when the flow rate of both air and hydrogen was increased.

In order to calculate the signal to noise ratio, the noise signals for each flow conditions were measured. The results are plotted in Fig. 6.3.

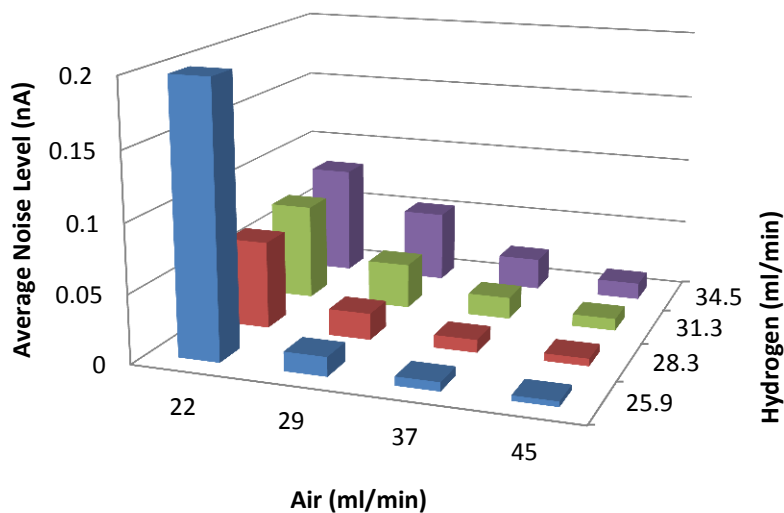


Figure 6.3 The plot shows the response noise signal for each flow conditions. Air was varied from 22 ml/min to 45 ml/min and hydrogen flow was varied from 25.9 ml/min to 34.5 ml/min and an oxygen flow half of the hydrogen flow was supplied.

As it can be determined from the graph in Fig. 6.3, the overall noise signal decreased with increasing flow rate of air at a constant hydrogen flow rate. On the other hand, the noise signal increased with higher flow rates of hydrogen. Higher hydrogen and oxygen flow rates resulted in producing higher flame temperature because of larger heat release. As a result, the electrical resistivity of the quartz plate decreased and the plates started to get electrically conductive [57]. This caused leakage current through the quartz plates and contributed to higher noise signals. Higher air flow contained more nitrogen and thus cooled the flame within the fixed hydrogen flow rate thus resulting in smaller leak current through the quartz plates. Noise level was abnormally high when the air flow rate was 22 ml/min and the hydrogen flow was 25.9 ml/min. This was because the flame was unstable (i.e. it flickered) at these low flow rates and produced strong noise

in the signals. Flame flickering occurred because at those small flow rates, flame heat release was not sufficient in order to overcome heat loss to the micro-burner hardware and the flames were driven close to extinction. This set a minimum flow-rate limit to achieve relatively low noise signals. These test results were used to calculate and determine the maximum signal-to-noise ratio within in the flow range tested. The optimal flow conditions to obtain that achieved the lowest possible MDL were determined as the minimum injection amount of analytes that can produce signals with a signal-to-noise ratio equal to two.

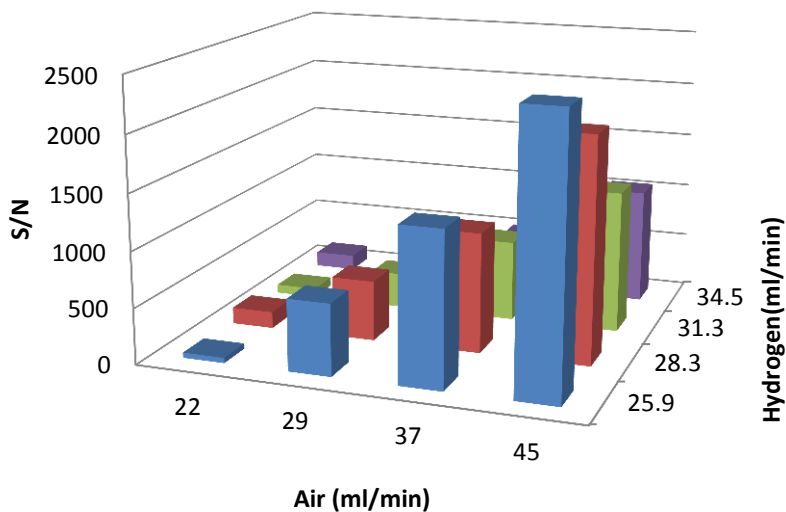


Figure 6.4 The plot shows the signal-to-noise ratio for each flow conditions. Air was varied from 22 ml/min to 45 ml/min and hydrogen flow was varied from 25.9 ml/min to 34.5 ml/min and an oxygen flow half of the hydrogen flow was supplied.

From the experimental results, the signal-to-noise ratio was calculated and presented in Fig. 6.4. Highest signal to noise ratio was achieved with high air flow (45 ml/min) and small hydrogen flow rates (25.9 ml/min). The increase of hydrogen and oxygen flow increased the overall flame temperature and resulted in higher ionization rate and increased the signal strength. However, the elevated temperature decreased the electrical insulation of the quartz plates and resulted in higher noise. Since, the noise levels differed by orders of magnitude while the actual strength of the signals did not vary much with flow parameters, higher signal-to-noise ratio was achieved with relatively low hydrogen and oxygen flow. The highest signal-to-noise ratio was achieved when 25.9 ml/min of hydrogen, 13 ml/min of oxygen, and 45 ml/min of air was supplied. This trend was observed within the introduced flow range, and could not be driven to infinity, since too much air and too little hydrogen will extinguish the flame.

At this point it is useful to introduce the air-fuel equivalence ratio λ .

$$\lambda = \frac{x_{O_2}/x_{H_2}}{x_{O_2,st}/x_{H_2,st}} = \frac{x_{O_2}/x_{H_2}}{1/2} = 2 \left(\frac{x_{O_2}}{x_{H_2}} \right) \quad (3)$$

Where, x_{O_2} is the mole fraction of oxygen and x_{H_2} is the mole fraction of the hydrogen. $x_{O_2,st}$, $(x_{H_2,st})$, are the mole fraction of oxygen (hydrogen) in a stoichiometric mixture with hydrogen (oxygen). Consequently, $\lambda = 1$ corresponds to a stoichiometric mixture while $\lambda > 1$ refers to oxygen rich conditions. It follows from our result in Fig. 6.4 that the signal-to-noise ratio increases with an increase of λ by raising the overall oxygen flow.

6.2 Determination of minimum saturation voltage

To create the electric field that is used for detection of the chemi-ions, a certain amount of voltage has to be applied to the electrodes. As voltage increases, the relation of collected charge to voltage is initially linear, however from one voltage on, the total charge has been collected and further increase in charge does not increase the recorded signal. The minimum voltage that can create an electric field that is strong enough to collect all the ions is defined as the saturation voltage. Increasing the magnitude of the applied voltage above the saturation level will not increase the signal. It is important to determine the saturation voltage in order to achieve strong signals. If the applied voltage on the electrodes is below the saturation voltage the electric field is not strong enough to collect all the chemi-ions. This can lead to loss of signal strength and deterioration of device performance.

Additionally, to achieve portability of the device, it has been a goal of this research that the entire system to be able to work with a portable battery. It is therefore important to minimize any unnecessary electric requirements. Verifying and applying the saturation voltage to the device will not only ensure full ion collection but also avoid any unnecessary power consumption and can diminish portability.

The experimental apparatus that was used in order to determine saturation voltage was similar to the experiment performed in chapter 3.4 (Fig 3.6). As shown in Fig 3.6, the micro-FID was connected to an external power supply that varied the applied voltage from 0 V until the signal saturated. In order to ignite and sustain the flame inside the

micro-FID, two mass flow controllers were used for the oxidizer and hydrogen flows. Methane was injected to the micro-FID in order to detect and compare the injection signals. An amount of 0.045 ml was injected for each applied voltage condition.

Figure 6.5 shows the maximum signal of the injection peak corresponding to the methane injection as the applied voltage varies. The amplitude rapidly increased till the applied voltage was around 40 V. The signal kept increasing till the applied voltage increases up to 100 V, where the ionization reached about its saturation point. The minimum driving voltage was around 100 V to extract most of the ions generated. Applied voltage lower than 100 V collected fewer ions and resulted in smaller and weaker signals. Based on this result, it was reasonable to set 100 V as the saturation voltage that can collect most ions during the sample injection.

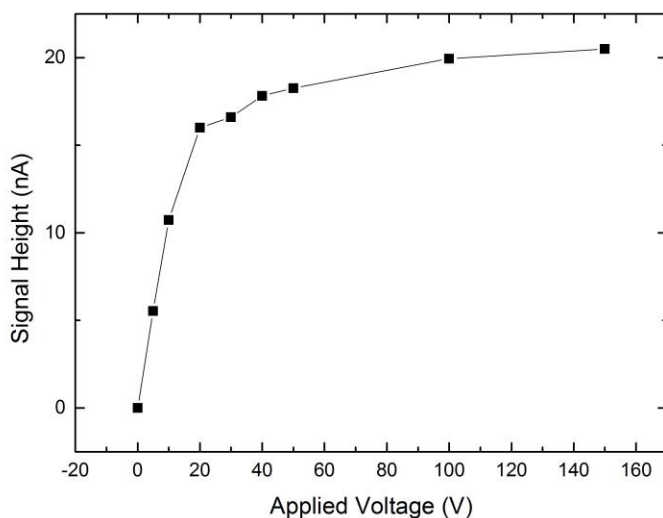


Figure 6.5. The plot shows the response signal in voltage of the injection peaks as the applied voltage is increased from 0 to 150V.

Chapter 7: Summary, Conclusions, and Recommendations for Future Work

7.1 Summary and Conclusions

The overarching goal of this research work was to develop a micro-FID using an encapsulated, well controlled diffusion flame which would be operated with low oxygen and hydrogen flow rates, that they could be achieved with water electrolysis with a small, commercially available battery. Thus, the initial stage of the research was focused on developing a micro-burner that could sustain a diffusion flame in a micro channel as described in chapter 2. The burner consisted of a quartz-silicon-quartz sandwich structure and encapsulated the air-hydrogen diffusion flame. In order to determine the optimal flame configuration, air and hydrogen were supplied in streams that converged with different angles to each other. Three different channel designs were tested with air and hydrogen channels that met with a 90° angle, 180° angle (counter-flow), and a 150° angle (folded flame channel design). The flame strain of the folded flame was about four times lower than the strain of the flame obtained with counter flow design. This suggested that the folded flame provided a more stable flame compared to the counter flow design. An additional advantage of this folded flame design was that it could confine the analytes between the two wings of the flame without losses due to extinction.

The reactive flow in the non-premixed flames encapsulated in the micro-FID was computed using ANSYS FLUENT. Nine different channel configurations were computed by changing the angle from 90° to 180° degree. The computations were

validated by the experimental observation and used in order to determine optimal channel configuration. The computational results showed that a singly connected, folded flame was established when the fuel and oxidizer streams intersected at an angle around 150° , which minimized analyte leakage. In addition, strain rates were calculated based on the computed velocity profile. It was determined that the strain rate decreased with increasing channel angle until a 170° angle was reached. Channel configurations between 150° - 170° produced relatively low strain rates. Therefore, in order to create channels for the micro-FID with minimum analyte loss and relatively low strain rates the channel angle should be designed around 150° - 160° .

Channels were designed and machined using Macor with a minimum channel thickness of $750\ \mu\text{m}$. The Macor channel was sandwiched together between two quartz plates. On each quartz plate, gold electrodes were fabricated in order to create the electric field for ion collection. The magnitude of the signal peaks was proportional to the amount of injection. Eventually, the two channel designs were tested and compared and showed that the ion collection with the folded flame channel design was about 34 times stronger than the counter-flow channel design. The folded channel design minimized the leakage of the analytes and had a smaller flame strain rate, which produced a more stable diffusion flame which resulted in producing stronger signals.

The results of chapter 3 established that the folded flame channel design was the desired channel configuration for the micro-FID. However, the sensitivity level of the developed micro-FID was still relatively low compared to commercial, large-scale FIDs and the overall fuel consumption rate was too high for portable applications. Thus,

subsequent work focused on modifying the micro-FID, so that it can be operated with a portable electrolyzer [55] that could produce an oxygen flow rate of 32 ml/min and hydrogen flow of 65 ml/min.

In order to reduce the overall fuel consumption rate, an oxygen stream from the electrolyzer was added to the air stream and the overall channel width size was reduced to 50%. Replacing a portion of the air flow to oxygen did not only reduce the overall flow rate, but also increased the overall flame temperature. During air-hydrogen combustion, the chemically inert nitrogen gas in the air dilutes the reactive oxygen. This results in heat loss and decrease in flame temperature. Therefore, replacing the air flow with oxygen increased the efficiency and sustained a flame with smaller flow rates. The oxidizer flow rate was reduced from 120 ml/min to about 40 ml/min, which was 3 time reduction in flow rate. Also, the hydrogen flow rate was reduced from 80 ml/min to 23 ml/min. Hydrogen and oxygen flow was supplied form a portable electrolyzer using a portable battery. The maximum hydrogen production of the electrolyzer was 65 ml/min with a water consumption of 0.05 ml/min [55]. To achieve the desired flow rates, the applied current to the electrolyzer was controlled. The micro-FID was operated with a hydrogen flow rate around 22 ml/min and required a current input of 1.9 A to 2.0 A. To our knowledge, this was the first demonstration of a “flame on a chip” that was fueled with the products of water electrolysis using a small portable battery.

Several tactics were introduced in chapter 4 to improve maximum signal strength, which essentially determined the capability of the micro-FID to detect hydrocarbon analytes and the MDL. It was established that longer residence times diminished the

maximum signal by distributing the total detected ion charge over a longer time period for a given amount of injection. Thus, the width of the injection channel was reduced in order to confine the injection gas and thus minimize residence time. Also, the dead volume between the injection port and the injection column was reduced. And finally an anchor point was embedded inside the channel to stabilize the flame and produce a sharper signal. These modifications allowed the device to operate with a portable electrolyzer.

Another approach to increasing sensitivity and the MDL was reducing noise. Instead of using Macor, the channels were fabricated with SOI wafers in order to provide better electrical insulation and prevent the melting of the Macor channels. Due to high flame temperature, channel regions close to the flame started melting and caused instability resulting in noise signals. By changing the material to silicon, the noise was reduced about 4 times. Additionally, operating the micro-FID inside a Faraday cage reduced noise by an additional factor of 43. This improvement of the device allowed successful detection and analysis of a mixture of the 17 compounds in the NASA Spacecraft Maximum Allowable Concentrations (SMAC) list [54].

In order to enable portability unnecessary battery loss needed to be minimized. Therefore, the saturation voltage was determined which is the minimum voltage that can create an electric field that is strong enough to collect all the ions. A quantity of 0.045 ml of methane was injected while varying the applied voltage to the electrodes. The signal corresponding to methane injection was measured while increasing the applied voltage. The signal amplitude rapidly increased till the applied voltage was around 40 V. The

signal kept increasing till the applied voltage increased up to 100 V. Based on experimental results, it was reasonable to set the applied voltage to 100 V which was verified as the saturation voltage.

Finally, in order to determine the flow conditions that can optimize flame stability and result in increasing the signal-to-noise ratio, characterization of the fuel flow rate was performed. The air flow rate was varied while the hydrogen flow rate was fixed and vice versa. Results showed that the signal strength increased with increasing hydrogen and oxygen flow while noise signal decreased with increasing air flow rates and decreasing hydrogen flow rates. Noise levels differed by orders of magnitude while the actual strength of the signals did not vary much with flow parameters. Therefore, higher signal-to-noise ratio was achieved with flow rates minimizing the noise level which was achieved when an air flow of 45 ml/min, a hydrogen flow of 26 ml/min, and an oxygen flow of 13 ml/min was supplied.

7.2 Outlook and Future work

A portable micro-FID has been developed that utilizes a diffusion flame encased in a micro-fabricated SOI structure and a portable electrolyzer that provides the hydrogen and oxygen flow rates necessary for the device operation. Different analytes such as methane, pentane, hexane, and benzene were used to make sure that the reported results were not analyte-specific, but a first step of future research should be to examine the new detector with a very wide range of chemicals.

The micro-FID could be operated with even lower fuel consumption by reducing the heat loss. Instability of the flame was observed when the fuel rate was reduced. In order to reduce the heat loss new material with low thermal conductivity such as aerogel is suggested. Hydrophobic aerogel materials could be used to avoid structural changes by vapor produced inside the micro-FID. Changing the quartz plates to aerogel will improve the insulation of the device and reduce the overall fuel consumption rate even more.

Due to its small size and low fuel consumption rate, the micro-FID can be integrated with micro-columns and micro-GCs. Separation of gas mixture inside columns needs temperatures higher than the boiling point of the gas analytes (otherwise they will condense inside the column and full separation will not occur). Thus, integration of the micro-FID with a micro-column can provide the heat needed using the heat released from the diffusion flame. This integrated micro-GC/ micro-FID system could potentially work as a standalone device for accurate gas analysis. In order to achieve integration of the devices, modifications might be needed to the gas ports.

However, during the development of the micro-FID it was determined that as long as the burner cavity maintained its' shape and angles, the channels guiding the gas flow did not have relatively little effect to the overall performance. Therefore, allowing the proposed micro-FID even more suitable for integration with other micro-sensing devices.

In addition, integration with other micro-detectors would take the device to another level. Since, the micro-FID is only sensitive to organic compounds the integration with an additional detector that can detect inorganic compounds would eliminate the detection limitation. For instance, integration with a Thermal Conductivity Detector (TCD) could be a viable way forward. The TCD is known to be able to detect both organic and inorganic compounds, however it is less sensitive than the FID. Thus the integrated device has the benefit of detecting inorganic compounds and still providing a high sensitivity to organic compounds.

Also, it has been suggested that the high energy density of hydrocarbon fuels provides a great opportunity to develop combustion based micro-power generation systems [25]. In order to meet increasing demands not only for chemical reactors and sensors, but for micro-power generation, micro-vehicles, micro-satellite thrusters the introduced micro-FID burner, which is a real “flame on the chip” can be modified and used in the context of micro-power generation and micro-propulsion.

Appendix A

A.1 Silicon Channel Fabrication

In this section, a step-by-step description of the silicon channel fabrication process used in section 2.3 is provided.

A.1.1 Patterning

1. A 4 inch DSP (Double side polished) silicon wafer was prepared and rinsed with Acetone, Isopropyl Alcohol (IPA), Deionized (DI) water, IPA, and dried with Nitrogen gas (N_2).
2. Silicon wafer was placed in the March Reactive Ion Etcher (RIE) and exposed to Oxygen plasma with 100 W power for 1 minute. (O_2 descum, $O_2:Ar = 2:1$)
3. Spin coat the top side of the wafer with Photoresist 4620 (PR) at 3000 RPM for 30 seconds.
4. Placed the wafer on a hot plate and soft backed at 60 °C for 2 minutes. Protected wafer by aluminum ring.
5. Placed the wafer on a hot plate and soft backed at 110 °C for 1 minute. Protected wafer by aluminum ring.
6. Cool the wafer on chuck for 1 minute.
7. Aligned the top side of the wafer to the design mask and exposed with a contact Aligner. (Exposed the photoresist to 405 nm wavelength (H-Line) UV light, at a power of 21.2 mW/cm² for 12 seconds (resulting exposure = 254.4 mJ/cm²))
8. Mixed 4:1 ratio of DI water and AZ 400K developer (100 mL DI water, 25 mL of AZ 400K).

9. Developed only two alignment marks using a pipette and dropping a few drops of AZ 400 K developer (4:1 of DI: developer) for about 2 minutes.
10. Checked the developed patterns under the microscope.
11. Expose backside with the same mask by back-side alignment with a contact Aligner. (Exposed the photoresist to 405 nm wavelength (H-Line) UV light, at a power of 21.2 mW/cm^2 for 12 seconds (resulting exposure = 254.4 mJ/cm^2)).
12. Placed the entire wafer in the 4:1 DI water and AZ 400K solution. Developed for about 2 minutes.
13. Mixed 10:1 ratio of DI water and AZ 400K developer (100 mL DI water, 10 mL of AZ 400K).
14. Placed the entire wafer in the 10:1 DI water and AZ 400K solution. Developed for about 1 minute.
15. DI quenched for 1 min, N_2 dry.
16. Checked the developed patterns under the microscope and proceed to step 14 if fully developed. Otherwise repeated step 12-14 and examine patterns.

A.1.2 Etching-ICP-DRIE (Inductively Coupled Plasma-Deep Reactive Ion Etcher)

1. Removed edge beads using acetone and swabs.
2. Baked the wafer on a hot plate at 135 °C for 7 minutes covered with Al foiled dish.
3. Ramped hot plate to 150 °C, and begun timing when hotplate reaches 150 °C for 15 min.
4. Loaded the wafer into the Plasmatherm Inductively Coupled Plasma Deep Reactive Ion Etcher (ICP-DRIE). Etched the wafer using the Bosch Process. Until its half way through.
5. Flipped the wafer over to the backside and loaded it with a carrier wafer in the ICP-DRIE. Etched the wafer using the Bosch Process until the alarm goes off.
6. Repeated about 20 loops and check if all the channels and holes are etched through, if not repeat another 20 loops; until all channels and holes are cleared
7. Placed the wafer into AZ 400T photoresist stripper on 120 °C hotplate for about 30 minutes.
8. DI quenched for 1 minute and rinsed it with DI water thoroughly.

Appendix B

In this section, a step-by-step description of the electrode fabrication process used in section 3.3 is provided.

B.1 Electrode Fabrication

1. Started with a 25.4 mm × 25.4 mm × 1.5748 mm quartz plates.
2. Spin coated the quartz plates with AZ1518 PR at 5000 RPM.
3. Placed the quartz plates on a hot plate and soft backed at 110 °C for 3 minutes.
4. Exposed the photoresist using the Flood expose for 6~8 seconds.
5. Mixed 4:1 ratio of DI water and AZ 400K developer (100 mL DI water, 25 mL of AZ 400K).
6. Placed the entire quartz plates in the 4:1 DI water and AZ 400K solution.
Developed for about 2 minutes.
7. Checked the developed patterns under the microscope.
8. DI quench for 1 min, N₂ dry
9. Quartz plates were placed in the March Reactive Ion Etcher (RIE) and exposed to Oxygen plasma with 100 W power for 1 minute. (O₂ descum, O₂:Ar=2:1)
10. Sputter Cr for 1 minute.
11. Sputter Gold for 4 minutes 15 seconds.
12. Placed the quartz plates into 1165PR stripper. (Lift-off)
13. DI quenched for 1 minute and rinsed it with DI water thoroughly.

Appendix C

In this section, a step-by-step description of the electrode fabrication process used in section 5.2 is provided.

C.1 Silicon Channel Fabrication (Flame folded flame)

C.1.1 Patterning

1. A 4 inch DSP (Double side polished) silicon wafer was prepared and rinsed with Acetone, Isopropyl Alcohol (IPA), Deionized (DI) water, IPA, and dried with Nitrogen gas (N_2).
2. Silicon wafer was placed in the March Reactive Ion Etcher (RIE) and exposed to Oxygen plasma with 100 W power for 1 minute. (O_2 descum, $O_2:Ar = 2:1$)
3. Spun 500 μ l of AP8000 (Adhesion Promoter) onto the polished side of the wafer. Spun at 3000 RPM for 30 seconds.
4. Spun 3000 μ l of SPR-220 Photoresist onto the polished side of the wafer. Spun at 3000 RPM for 30 seconds
5. Placed the wafer on a hot plate and soft backed at 60 $^{\circ}C$ for 2 minutes. Protected wafer by aluminum ring.
6. Placed the wafer on a hot plate and soft backed at 110 $^{\circ}C$ for 1 minute. Protected wafer by aluminum ring.
7. Cool the wafer on chuck for 1 minute.

8. Aligned the top side of the wafer to the design mask and exposed with a contact Aligner. (Exposed the photoresist to 405 nm wavelength (H-Line) UV light, at a power of 21.2 mW/cm^2 for 12 seconds (resulting exposure = 254.4 mJ/cm^2))
9. Mixed 4:1 ratio of DI water and AZ 400K developer (100 mL DI water, 25 mL of AZ 400K).
10. Developed only two alignment marks using a pipette and dropping a few drops of AZ 400 K developer (4:1 of DI: developer) for about 2 minutes.
11. Checked the developed patterns under the microscope.
12. Expose backside with a second mask by back-side alignment with a contact Aligner. (Exposed the photoresist to 405 nm wavelength (H-Line) UV light, at a power of 21.2 mW/cm^2 for 12 seconds (resulting exposure = 254.4 mJ/cm^2)).
13. Placed the entire wafer in the 4:1 DI water and AZ 400K solution. Developed for about 2 minutes.
14. Mixed 10:1 ratio of DI water and AZ 400K developer (100 mL DI water, 10 mL of AZ 400K).
15. Placed the entire wafer in the 10:1 DI water and AZ 400K solution. Developed for about 1 minute.
16. DI quenched for 1 min, N_2 dry.
17. Checked the developed patterns under the microscope and proceed to step 14 if fully developed. Otherwise repeated step 12-14 and examine patterns.

C.1.2 Etching-STS Pegasus DRIE (Deep Reactive Ion Etcher)

1. Loaded the wafer top side up into the STS Pegasus deep reactive ion etching machine and ran a faster Bosch process to etch only several microns.
2. Unloaded the wafer and placed it on a carrier wafer backside facing up using crystal wax.
3. Loaded wafer in to the STS DRIE. Etched through using a faster Bosch Process.
4. Unloaded the wafer from the STS DRIE and soaked it into DI water to remove the crystal wax.
9. Placed the wafer into AZ 400T photoresist stripper on 120 °C hotplate for about 30 minutes.
10. DI quenched for 1 minute and rinsed it with DI water thoroughly.

C.1.3 Cleaning

C.1.3.1 Cleaning (Piranha)

1. Mix 3:1 of sulfuric acid (120ml) and hydrogen peroxide (40ml). (Important: always add 'peroxide' to 'acid'! In the other way, the solution may explode.)
2. Placed the wafer into the Piranha solution.
3. Moved the solution to the hotplate and set the hotplate temperature to 150 °C and heat it up for 15minutes.
4. Moved to solution to the side and waited a couple of minutes to cool down.
5. Took the wafer out and DI quenched for 2 minute and rinsed it with DI water thoroughly.

C.1.3.2 Cleaning (SC-1)

1. Prepared the SC-1 solution (DI water 200 ml, Hydrogen Peroxide 20 ml, Ammonium Hydroxide 2ml (or 58 drops)) and heated hotplate to 150 °C.
2. Transferred the wafer to SC-1 solution on hotplate.
3. Set hotplate probe to 75 °C, ramped and soaked the wafer for 30 minutes.
4. Transferred the wafer into the 1:1 DI water and IPA solution (100 /100 ml) for 2 minutes.
5. DI quenched for 1 minute and rinsed it with DI water thoroughly.

C.1.4 Growing Thermal Oxide Layer (Electrical Insulation Layer)

1. Made sure the O₂ is off and turn on N₂ from 2.5 L/min to 6 L/min.
2. Set the temperature of the oxidation furnace tube to 1100 °C.
3. Waited until the temperature is at least 900 °C before loading the samples.
4. Loaded samples once the tube furnace temperature was around 900 °C.
5. Took out the quartz boat with the clamp (left the boat inside the tube), put samples on the quartz boat, and placed the quartz boat on the mouth of the tube.
Waited about 2 minutes at the mouth of the furnace tube.
6. Pushed the boat in to the center of the tube very slowly.
7. Waited until the temperature reaches set temperature 1100 °C.
8. Changed gas by turning on O₂ flow to 6 L/min and then turned off N₂ flow.
9. Grew oxide for 1hr at 1100 °C with O₂ flow at 6 L/min (~1000Å)
10. Cooled the oxidation tube to 600 °C and unload the wafer
11. Prepared Buffered Oxide Etchant (BOE) in a PTFE container. Placed the wafer polished side up into the BOE solution for 2 minutes and 30 seconds and removed all oxide in BOE. Submerged the wafer in a DI water bath for 1 minute 30 seconds.
12. Loaded wafer into the oxidation tube about 900 °C and then heat to 1100 °C. Grew oxide for 13.5hrs at 1100 °C with O₂ flow at 6 ml/min (~5000Å)

References

- [1] T.Holm, "Aspects of the mechanism of the flame ionization detector", *Journal of Chromatography A*, vol. 842, pp. 221-227, 1999.
- [2] S. Zimmermann, P. Krippner, A. Vogel and J. Müller, "Miniaturized flame ionization detector for gas chromatography", *Sensors and Actuators, B: Chemical*, vol. 83, pp. 285-289, 2002.
- [3] C. Washburn, M. W. Moorman, T. W. Hamilton, A. L. Robinson, C. Mowry, R. G. Manley, G. Shelmidine and R. P. Manginell, "Micro-flame ionization detection using a catalytic micro-combustor," in *Proceedings of IEEE Sensors*, 2005, pp. 322-325.
- [4] Raymond P. W. Scott , "Gas Chromatography Detectors", Chrom-Ed Book Series, Book 4, 2003, libraryforscience, LLC
- [5] D.G.McMinn, H.H.Hill, in : H.Hill, D.G.McMinn (Eds), *Detectors for Capillary Chromatography*, John Wiley & Sons, New York, 1992
- [6] C. Washburn, M. W. Moorman, T. W. Hamilton, A. L. Robinson, C. Mowry, R. G. Manley, G. Shelmidine and R. P. Manginell, "Micro-flame ionization detection using a catalytic micro-combustor," in *Proceedings of IEEE Sensors*, pp. 322-325, 2005.
- [7] W.Kuipers, J. Müller, "Sensitivity of a planar micro-flame ionization detector", *Talanta*, vol. 82, pp. 1674-1679, 2010.
- [8] W. J. Kuipers and J. Müller, "Charaterizaton of a microelectromechanical systems-based counter-current flame ionization detector", *Journal of Chromatography A*, vol. 1218, pp.1891-1898, 2011.
- [9] R. A. Dewar, "The flame ionization detector a theoretical approach", *Journal of Chromatography A*, vol. 6, pp. 312-323, 1960.
- [10] K. Schofield, "The enigmatic mechanism of the flame ionization detector: Its overlooked implications for fossil fuel combustion modeling", *Progress in Energy and Combustion science*, vol.34, pp.330-350, 2008
- [11] T. Holm, J. Ø. Madsen, "Methane Formation by Flame-Generated Hydrogen Atoms in the Flame Ionization Detector", *Anal. Chem.*, 1996, 68 (20), pp 3607–3611
- [12] J. Sevcik, "Detectors in gas chromatography", *Journal of Chromatography Library*, vol. A, pp. 94-95, 1975.

- [13] M. Moorman, R. P. Manginell, C. Colburn, D. Mowery-Evans, P. G. Clem, N. Bell and L. F. Anderson, "Microcombustor array and micro-flame ionization detector for hydrocarbon detection," in *Proceedings of SPIE - the International Society for Optical Engineering*, pp. 40-50, 2003.
- [14] W. J. Kuipers and J. Müller, "A planar micro-flame ionization detector with an integrated guard electrode," *J Micromech Microengineering*, vol. 18, pp. 1-7, 2008.
- [15] S. Zimmermann, S. Wischhusen and J. Müller, "Micro flame ionization detector and micro flame spectrometer," *Sensors and Actuators, B: Chemical*, vol. 63, pp. 159-166, 2000.
- [16] J.F Franklin, "Mass Spectrometric Studies of Chemionization by Reaction of Electronically Excited Species", in; *Mass Spectrometry in Inorganic Chemistry*; Margrave, J; *Advances in Chemistry*; American Chemical society, Washington, DC, 1968
- [17] Davy, H., "An account of an invention for giving light in explosive mixtures of fire-damp in coal mines, by consuming the fire-damp," *Philosophical Transactions*, **23**, 114, 1814.
- [18] Deng, W. et al. "Liquid Fuel Combustor Miniaturization via Microfabrication", *Proceedings of the Combustion Institute*, Vol. 31, pp.2239-2246, 2006.
- [19] A.C. Fernandez-Pello, "Micro-Scale Power Generation Using Combustion: Issues and Approaches" *Proceedings of the Combustion Institute*, vol. 29, pp.883-899, 2002
- [20] A.C. Fernandez-Pello, "Micro-Scale Combustion: Issues, Applications and Progress", *Proceedings of the Third Mediterranean Combustion Symposium*, Marrakech, Morocco, June 8-13, C6.1-C6.6, 2003.
- [21] J. Peck, S. A. Jacobson, and I.A. Waitz, "Design and Characterization of a liquid-fueled micro-combustor", *Proceedings of ASME Turbo Expo 2010: Power for Land, Sea and Air*, GTP-10-1106, June 14-18, 2010, Glasgow, UK, *J. Engineering For Gas Turbines and Power*, vol. 133 (7), 2011.
- [22] C. M. Spadaccini and I.A. Waitz , "Microcombustors for Rotating Machinery," chapter in *Multi-Wafer Rotating MEMS Machines*, J.H. Lang (ed.), MEMS Reference Shelf, 445 DOI 10.1007/978-0-387-77747-4_9, C _ Springer Science+Business Media, LLC 2009

- [23] C. M. Spadaccini, J.W. Peck, and I. A. Waitz, "Catalytic Combustion Systems for Micro-Scale Gas Turbine Engines," GT2005-68382, *Proceedings of the ASME Turbo Expo*, June, 2005
- [24] C. M. Spadaccini, X. Zhang, C. P. Cadou, N. Miki, and I. A. Waitz, "Development of a Catalytic Silicon Micro-Combustor for Hydrocarbon-fueled Power MEMS," *Sensors and Actuators*, vol. A (103), pp. 219–224, 2003.
- [25] Y. Ju, K. Maruta, "Microscale combustion: Technology development and fundamental research", *Prog. Energy and Combust.Sci.* vol. 37, pp. 669-715, 2011
- [26] A. Mehra and I. A. Waitz , "Development of a Hydrogen Combustor for a Microfabricated Gas Turbine Engine," *1998 Solid State Sensor and Actuator Workshop*, Hilton Head Transducers Conference, June 2-4, 1998.
- [28] B. Xu and Y. Ju, "Numerical Modeling of the Heterogeneous Combustion in a Micro Scale Chemical Reactor," AIAA-2004-304, 42nd AIAA Aerospace Sciences Meeting and Exhibit, Reno, Nevada, Jan. 5-8, 2004.
- [29] B. Xu and Y. Ju, "Concentration slip and its impact on the heterogeneous combustion in a microscale chemical reactor," *Proc. of Eastern States Section Meeting of the Combustion Institute*, Penn. State Univ., 2003
- [30] B. Xu And Y. Ju, "Rarefied Gas Effect On Concentration Slip And Catalytic Reaction In Microscale Reactors," *Chemical Engineering Science*, vol. 60, pp. 3561-3572, 2005.
- [31] Heatwole, S., Veeraragavan, A., Buckley, S., and Cadou, C., "In-situ Species and Temperature Measurements in a Micro-combustor", *Journal of Nanoscale and Microscale Thermophysical Engineering*, vol. 13, pp. 1-23, 2009.
- [32] Heatwole, S., Veeraragavan, A., Buckley, S., and Cadou, C., "In-situ Species and Temperature Measurements in a Micro-combustor", *Journal of Microscale Thermophysical Engineering*, June 2005.
- [33] C.M. Spadaccini, X. Zhang, C.P. Cadou, N. Miki, and I.A. Waitz, "Preliminary Development of Hydrocarbon-Fueled Catalytic Micro Combustor," *Sensors and Actuators*, vol. A 103 (1-2), pp. 219-224, 2003
- [34] Smyth S. A., K. T. Christensen, and D. C. Kyritsis, "Intermediate Reynolds Number Flat Plate Boundary Layer Flows over Catalytic Surfaces for "Micro"-

- Combustion Applications,” *Proceedings of the Combustion Institute*, 32, 3035-3042, 2009.
- [35] Miesse, C. M., C. J. Jensen, R. I. Masel, M. A. Shannon, and M. Short, "Sub-millimeter Scale Combustion," *AICHE Journal*, **50**: 12 , 3206, 2004
- [36] Miesse, C. M., R. J. Masel, M. Short, and M. A. Shannon, "Experimental Observations of Methane-Oxygen Diffusion Flame Structure in a Sub-millimeter Microburner," *Combustion Theory and Modeling*, Institute of Physics Publishing, Ltd. **9**, 77-92, 2005
- [37] Prakash, S., A. Armijo, R. Masel, and M. A. Shannon, "Flame dynamics in sub-millimeter combustors," *Int. J. Alternative Propulsion* ,**1**(2/3), 325-338, 2007
- [38] J.Wang, H.Wang, C,Duan, Y.Guan, “Micro-flame ionization detector with a novel structure for portable gas”, *Talanta*, vol. 82, pp. 1022-1026, 2011
- [39] T. C. Hayward, K.B. Thurbide, "Move on-column inverted operating modes of a microcounter-current flame ionization detector”, *Journal of Chromatography*, vol. A, pp. 2-7, 2008
- [40] T. C. Hayward, K.B. Thurbide, "Carbon response characteristic of a micro-flame ionization detector”, *Talanta*, vol. 82, pp. 583-588, 2007
- [41] C. Miesse, R. Masel, M. Short, M. Shannon, “Diffusion flame instabilities in a 0.75 mm non-premixed microburner”, *Proc.Combust.Inst.*, vol. 30, pp. 2499-2507, 2005
- [42] D. R. Reyes, D. Iossifidis , P. Auroux , A. Manz, “Review Micro Total Analysis Systems. 1. Introduction, Theory, and Technology”, *Anal. Chem.*, vol. 74 (12), pp. 2623–2636, 2002
- [43] G. Lambertus, A. Elstro, K. Sensenig , J. Potkay, M. Agah , S. Scheuering, K. Wise, F. Dorman, R. Sacks, “ Design, Fabrication, and Evaluation of Microfabricated Columns for Gas Chromatography”, *Anal. Chem.*, vol. 76 (9), pp. 2629-2637, 2004
- [44] J. J. Whiting, C. Lu, E. T. Zellers, R. D. Sacks, “A Portable, High-Speed, Vacuum-Outlet GC Vapor Analyzer Employing Air as Carrier Gas and Surface Acoustic Wave Detection”, *Anal. Chem.*, vol. 73 (19), pp. 4668-4675, 2001
- [45] J.A. Dziuban, J. Mróz, M. Szczygielska, M. Małachowski, A. Górecka-Drzazga, R. Walczak, W. Buła, D. Zalewski, Ł. Nieradko, J. Łysko, J. Koszur, P. Kowalski , “ Portable gas chromatograph with integrated components”, *Sensors and Actuators A: Physical*, vol. 115 (2-3), pp. 318-330, 2004

- [46] E. B. Overton, K. R. Carney, N. Roques, H. P. Dharmasena, "Fast GC instrumentation and analysis for field applications", *Field Anal. Chem. Technol.*, vol. 5 (1-2), pp. 97-105, 2001
- [47] S.P.Burke and T.E.W.Schumann, "Diffusion flames", Proceedings of the Combustion Institute, vol 1, pp.2-11, 1948
- [48] M.J.Madou, "Fundamentals of Microfabrication", CRC, pp.2-6, 2001
- [49] B. Bae, J. Kim, M. Shannon, T. Kang, U.S.Patent (pending) Application No. 13/801,949
- [50] K. Seshadri and F.A. Williams, "Laminar flow between parallel plates with injection of a reactant at high Reynolds number", *International Journal of Heat and Mass Transfer*, vol.21, pp. 251-253, 1978.
- [51] J. Kim, B. Bae, J. Hammonds, T.Kang, M. Shannon, *Sensors and Actuators B: Chemical*, 168, (2012) 111–117.
- [52] <http://en.wikipedia.org/wiki/Vespel> - accessed Nov. 2011.
- [53] W. A. Aue, H. Singh, X. Sun, "Fundamental noise in three chromatographic detectors", *Journal of Chromatography, A*, vol. 687, pp. 283-290, 1994.
- [54] Spacescraft Maximum Allowable Concentrations for Airborne Contaminant - <http://www.cdc.gov/niosh/docket/archive/pdfs/NIOSH-125/125-NASAJSC205841999.pdf>
- [55] <http://www.fuelcellstore.com/en/pc/viewPrd.asp?idproduct=1269&idcategory=60>
- [56] B. Bae, J. Kim, J. Yeom, Q. Chen, C. Ray, and M. Shannon, "Development of a portable gas analyzer using a micro-Gas Chromatograph/Flame Ionization Detector (micro-GC/FID) for NASA's environmental missions," 42nd Int. Conf. on Environmental Systems (ICES), San Diego, CA, USA, 2012 AIAA 2012-3435.
- [57] H. E. Seemann, "The thermal and electrical conductivity of fused quartz as a function of temperature", *Phys. Rev.* vol. 31, pp. 119–129, 1928.